

CONSTRAINTS ON THE APHELION CLOUD BELT PHASE FUNCTION WITH MARS SCIENCE  
LABORATORY (MSL) AND MARS COLOR IMAGER (MARCI)

BRITTNEY COOPER

A THESIS SUBMITTED TO THE FACULTY OF GRADUATE STUDIES IN PARTIAL  
FULFILLMENT OF THE REQUIREMENTS FOR THE DEGREE OF

MASTER OF SCIENCE

GRADUATE PROGRAM IN EARTH AND SPACE SCIENCE  
YORK UNIVERSITY  
TORONTO, ONTARIO

September, 2019

© Brittney Cooper, 2019

# Abstract

We constrained the phase function of Martian water ice clouds (WICs) in the aphelion cloud belt season using data from both Mars Science Laboratory (MSL), and the Mars Color Imager (MARCI). The modeled ice crystal phase functions which best fit our derived results were aggregates (with p-values ranging from 0.908-0.940 for MARCI, and 0.60 for MSL), closely followed by bullet rosettes and columns, while the least likely were spheres (0.399-0.454 for MARCI and 0.2 for MSL). Additionally, this work probed the opposition surge to examine the Martian atmosphere's relationship between ice water content and extinction, and found it to be less than was previously proposed for particles at the Phoenix landing site by a factor of 2, with a large dependence upon particle radius. Half-width-half-maximums of the  $180^\circ$  peak in five MARCI images were analyzed and compared to models for WICs and found to agree better than those for dust.

# Dedication

This work is dedicated to my mother, and the memory of my grandfather.

# Acknowledgements

I would like to convey my deepest thanks and appreciation to my supervisor, Professor John Moores, for his immense support and encouragement from early on. The opportunities and experiences I encountered as both an undergraduate and graduate researcher in his lab allowed me to grow academically, professionally, and personally over these last 5 years. It has been an honour and a pleasure to have been his student and learn by example what it means to be a thoughtful, supportive, and driven scholar.

I would also like to thank the Mars Science Laboratory (Curiosity Rover) science and operations teams for their support of this work and the operational implementation of the Phase Function Sky Survey. As well, the Curiosity engineering cameras team, especially Doug Ellison for designing the Phase Function Sky Survey, and then re-designing it (playfully dubbed the “All-Sky-Neck-Snapper 2.0”) when it faulted on the rover.

A big thank-you to Scott Guzewich for his contributions to this work by providing the Mars Climate Sounder ice and dust opacity profiles necessary for the phase function calculations, and helpful feedback and comments on the two manuscripts that make up this thesis. As well, Michael Battalio for serving as the inspiration to get back to the Mars Color Imager dataset, and providing spatial and temporal maps of Martian dust events that greatly improved the quality of our analysis.

Finally, I would like to thank my husband Tom and my family for their constant love and support (without which I couldn’t imagine accomplishing much of anything). Also to my friends and my peers (especially the members of the Planetary Volatiles Lab) thank-you for all your help, what a pleasure to have worked alongside you all.

# Table of Contents

Abstract .....	ii
Dedication.....	iii
Acknowledgements.....	iv
Table of Contents .....	v
List of Figures.....	vii
1. Introduction .....	1
1.1 Atmospheric Water on Mars.....	1
1.2 The Aphelion Cloud Belt.....	2
1.3 Cirrus Clouds as an Analog for Martian WICs.....	5
1.4 Scattering Phase Function and Ice Crystal Geometries.....	6
1.5 Constraints on the Phase Function and Ice Crystal Habits of Martian WICs.....	13
1.6 Organization of Thesis.....	16
2. MSL Dataset and Analysis Methods.....	17
2.1 MSL Navcam Phase Function Sky Survey.....	17
2.2 Deriving the Phase Function from MSL Navcam Imagery.....	19
3. MSL Dataset Results and Analysis.....	27
3.1 MSL Navcam Phase Function Sky Survey Results.....	27
3.2 Comparison of PFs to Known Ice Crystal Geometries.....	30
3.3 Comparison of PFs to Other Phase Functions for Martian WICs.....	36
3.4 Cloud Features.....	40
4. MARCI Data Calibration and Methods.....	42
4.1 Radiometric Calibration.....	42

4.2	Phase Function Determination.....	46
5.	MARCI Dataset Results.....	51
5.1	Spectral Phase Function.....	51
5.2	Geographic Analysis.....	53
5.3	Seasonal Analysis.....	60
6.	MARCI Data Discussion.....	66
6.1	A Closer Look at the Opposition Surge.....	66
6.2	Phase Function Normalization and Habit Analysis.....	71
7.	Conclusions.....	79
	Bibliography.....	84

# List of Figures

1.1	A Hubble Space Telescope image of Mars highlighting the ACB .....	2
1.2	The observed cloud opacities from MSL for Mars Years (MYs) 31, 32, and 33.....	3
1.3	THEMIS retrieved water ice optical depths at $825\text{cm}^{-1}$ .....	4
1.4	Phase functions from Viking data and modeled phase functions of nine ensembles containing.....	8
1.5	Visual examples of scattering phenomena.....	9
1.6	Lidar contour plot showing the detection of Martian WICs and precipitation.....	10
1.7	Bright “subsun” in image captured by MOC.....	12
1.8	A low resolution constraint of the lower bound of the Martian WIC phase function.....	14
2.1	Projections of PFSS frame pointings on a dome.....	18
2.2	Example of the two tiers of PFSS frames at each of the nine observation pointings.....	19
2.3	A visual representation of the phase function redirecting incident radiation.....	21
2.4	An example of the MFS time-variable component.....	24
3.1	The temporal distribution of the 35 PFSS runs.....	27
3.2	The mean curve of the derived phase function data.....	29
3.3	The normalized mean curve of our results, along with the 7 modeled phase functions.....	31
3.4	Histograms of the residuals from the phase function data.....	34

3.5	The mean and upper bound of our normalized results alongside composite RT model and EPF derived phase functions.....	37
3.6	Histograms of the residuals from the phase function data.....	38
3.7	Cloud Features in perturbation images from a single pointing in a PFSS observation.....	40
4.1	Schematic of the typical viewing geometry of MARCI with MRO in its 3 am/3 pm sun-synchronous orbit.....	44
4.2	Cross-track reflectances produced using our methods along a single row.....	45
4.3	A two dimensional diagram depicting the physical relevance of the cosine of the emission and solar zenith angle.....	49
5.1	The point densities of the filtered, unnormalized phase function data.....	52
5.2	Phase function data plotted with respect to their latitude and longitude.....	55
5.3	Phase function point densities for the blue and red filters were separated into two latitude ranges across all seasons.....	58
5.4	Phase function point densities were produced for the blue filter over solar longitude ranges.....	61
5.5	Phase function values for the red and blue filters are plotted with respect to Martian latitude and solar longitude.....	63
6.1	Cropped RGB MARCI images from the ACB season.....	69
6.2	The five seasonal mean phase functions.....	71

6.3	The normalized mean seasonal phase functions were compared to seven modeled ice crystal phase functions.....	73
6.4	The normalized seasonal phase functions were compared to the mid-latitude and polar phase functions.....	75

# Chapter 1

## Introduction

### 1.1 Atmospheric Water on Mars

Although 10,000 times less abundant on Mars than Earth, water vapor is a powerful and dynamic trace gas in the Martian atmosphere (Maltagliati et al., 2011). Approximately ten percent of the total water vapour in the Martian atmosphere contributes to the seasonally-driven formation of water ice clouds (WICs) through saturation and deposition at equatorial regions, as well as the formation of WICs driven by atmospheric waves and dynamics near the poles.

The significance of Martian WIC's was initially down-played following the unusually warm and dusty Viking era observations of the 1970's (Tamppari et al., 2000), and this led to Martian WICs remaining greatly underappreciated until the 1990's when the Aphelion Cloud Belt (ACB) was discovered (Clancy and Lee, 1991). The global scale (as observed in Figure 1.1), duration, and year-to-year repeatability of the ACB led to new speculation and investigation into the range of physical and thermal impacts of Martian water ice clouds on the atmosphere and climate.

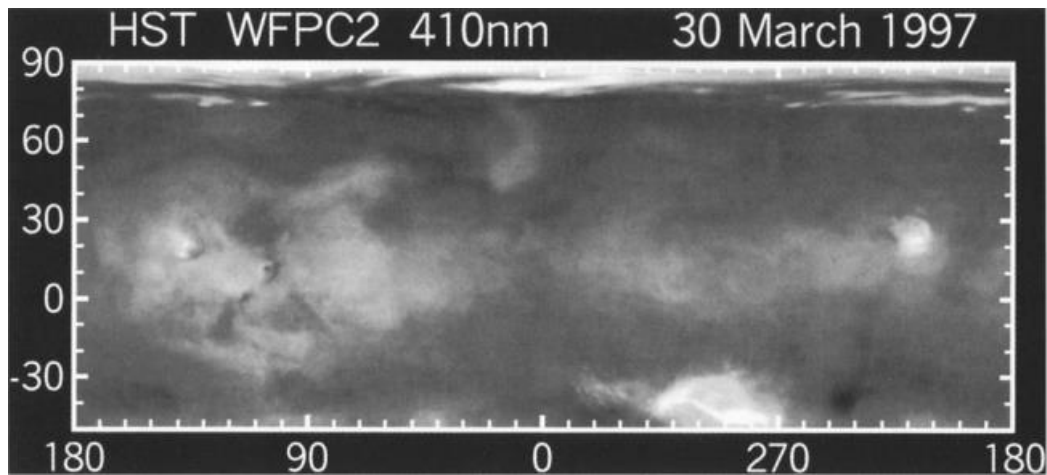


*Figure 1.1: A Hubble Space Telescope image of Mars highlighting the ACB, as observed in 1997 at a wavelength of 410nm (Malin et al., 2009). The brightest pixels within the lower latitudes in this image are the clouds that make up the ACB during the aphelion season.*

## 1.2 The Aphelion Cloud Belt

Mars has an orbital eccentricity of 0.0934 (Simon et al., 1994), so its position in orbit around the Sun has a noticeable impact on its seasonal meteorology and climate. As Mars approaches its greatest distance from the Sun at aphelion around a solar longitude of  $L_s = 71^\circ$  (a measure of Mars' position in orbit where  $0^\circ$  corresponds to the vernal equinox in the northern hemisphere), the planet's atmosphere cools and a decrease in dust lifting is observed along with a marked increase in cloud formation and density. Figure 4 from Kloos et al. (2018)

demonstrates the seasonal peak in cloud opacities as observed by Mars Science Laboratory (MSL), spanning approximately  $L_s=50^\circ-180^\circ$  over multiple Martian years. As Mars approaches the northern hemisphere's autumnal equinox at  $L_s =180^\circ$ , the atmosphere begins to warm and active dust lifting resumes while cloud formation declines (Newman et al., 2005). The decrease in cloud formation continues as Mars reaches and surpasses its closest approach of the Sun at perihelion, at  $L_s=250^\circ$ . This process repeats annually and gives rise to the phenomenon known as the Aphelion Cloud Belt.

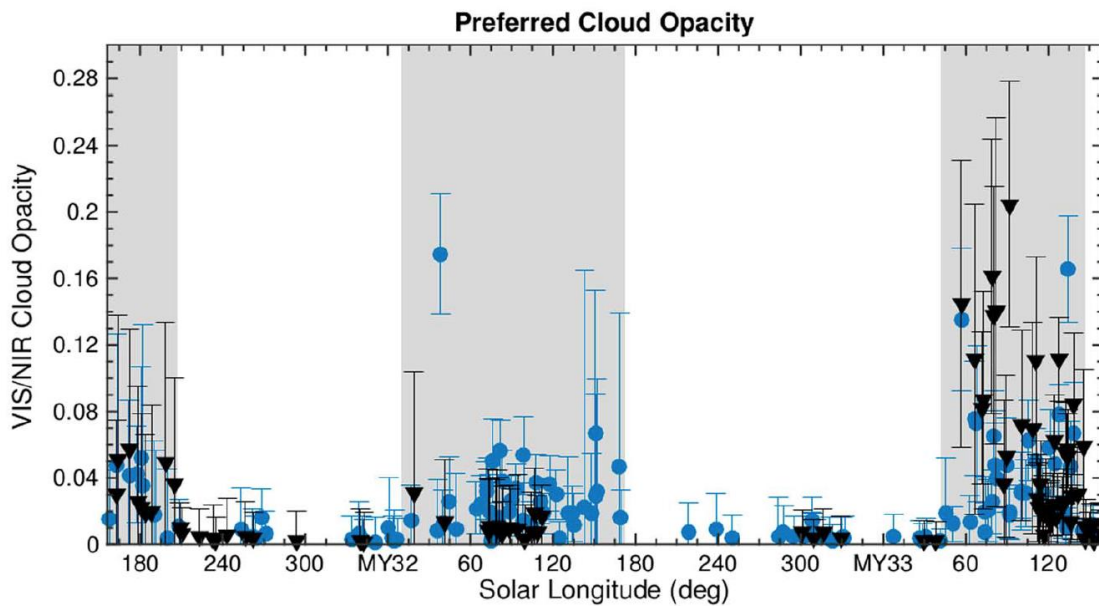


Figure 1.2: The observed cloud opacities from MSL for Mars Years (MYs) 31, 32, and 33 (Kloos et al., 2018) show the peak opacities occur on an annual basis within the aphelion season (approximately  $L_s=50^\circ-180^\circ$ ).

The ACB typically extends from  $-10^{\circ}$  to  $30^{\circ}$  latitude, with a range of optical depths ( $\tau$ ) from 0.05-0.5 (Wolff et al., 1999) spanning  $L_s = 70^{\circ} - 180^{\circ}$  (Smith, 2009). With such a broad geographical and temporal extent, the ACB offers an annually re-occurring opportunity to study a variety of Martian WICs, both globally and locally. As a result, there has been great interest in the last two decades to map and characterize Martian WICs, as well as to conduct retrievals of cloud physical properties.

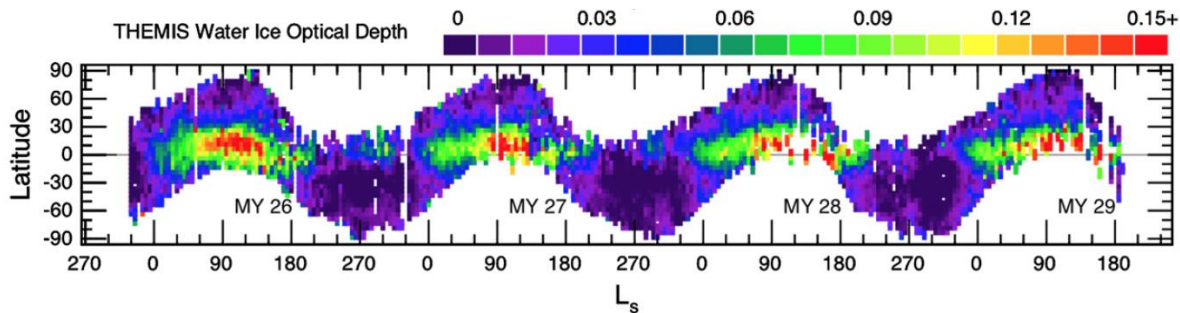


Figure 1.3: THEMIS retrieved water ice optical depths at  $825\text{cm}^{-1}$  show the spatial and temporal repeatability of the ACB over four MYs (Smith, 2009).

Globally, these investigations have utilized the Thermal Emission Imaging Spectrometer (THEMIS) aboard Mars Odyssey, as seen in Figure 1.3 (Smith, 2009), the Mars Color Imager (MARCI), the Mars Climate Sounder (MCS) (Kleinböhl et al., 2009), and the Compact Reconnaissance Imaging Spectrometer for Mars (CRISM) (Guzewich et al., 2014) aboard the Mars Reconnaissance Orbiter (MRO), the IR Mapping spectrometer OMEGA aboard Mars Express (Madeline et al., 2012b), and Mars Orbiter Camera (MOC) and Thermal Emission Spectrometer (TES) aboard Mars Global Surveyor (MGS) (Clancy et al., 2003). These analyses have returned

cloud and haze optical depths, ice crystal particle sizes, cloud morphologies and qualitative classifications.

From the surface, Mars Pathfinder (Smith & Lemmon, 1999), the Mars Exploration Rovers (Lemmon, 2004), the Phoenix Lander (Whiteway et al., 2009 and Moores et al., 2010) and Mars Science Laboratory (Moores et al., 2015 and Kloos et al., 2016) have also completed extensive high-resolution local observations. These surface studies have led to the discovery of precipitation and near-surface fog on Mars (Whiteway et al., 2009, Moores et al., 2011), as well as an understanding of how cloud optical depths vary seasonally, and diurnally (Wilson et al., 2007; Kloos et al., 2018).

### 1.3 Cirrus Clouds as an Analog for Martian WICs

Many parallels can be drawn between terrestrial cirrus clouds and Martian WICs, as both are clouds composed of frozen water ice deposited onto cloud condensation nuclei (CCN) with temperatures well below 273 K. They are formed in similar conditions, as the Martian troposphere has similar temperatures and pressures to the Terrestrial stratosphere (Petrosyan et al., 2011). For nucleation in the presence of CCN, only slightly supersaturated conditions are required for nucleation (Comstock et al., 2008), making that the likely scenario for WIC formation on both Earth and Mars.

On Earth, cirrus clouds have a large impact on the global radiation budget, as they contribute to a warming greenhouse effect by absorbing infrared (IR) radiation emitted from the surface and re-emitting it into the atmosphere. They also reflect a

great deal of solar radiation back out to space, thereby producing a cooling effect (Poetzsch-Hefter et al., 1994). When the sum of these effects is tallied, cirrus clouds are found to be the only terrestrial cloud that has a net warming effect on Earth's radiation budget, as they are nearly transparent in the visible range of wavelengths, but optically thick in the infrared.

Similar effects from Martian WICs have been investigated and modeled, finding the average effect to be net cooling below 15 km and net warming above (Madeleine et al., 2012), but models are still struggling to constrain the cloud microphysics to properly output what is being observed in sounder profiles. Schlimme et al. (2005) demonstrated that in the case of terrestrial water ice clouds, the most sensitive parameters for modelling the solar broadband radiative transfer of clouds are (in order of importance): optical thickness, ice crystal shape, ice particle size, and spatial structure. If any of these parameters, let alone the most sensitive ones, are not well constrained, the model will be impaired.

## 1.4 Scattering Phase Function and Ice Crystal Geometries

One aspect of Martian WICs that has yet to be thoroughly investigated via direct observation from the surface is the scattering phase function. The phase function is a parameter that describes the angular distribution of scattered radiation from a scattering center. Because the WIC phase function is determined by the shape of the ice crystals within the WICs, it can be used to constrain the dominant geometries of those ice crystals.

Publications that span from the Viking era to present day have largely utilized a method of fitting radiative transfer (RT) models to emission phase function (EPF) data taken over a finite range and resolution of emission angles (Pollack et al., 1979, Clancy and Lee, 1991, Clancy et al., 2003, Wolff et al., 2009). When the resultant phase functions are plotted against their respective scattering or phase angles, they typically produce flat curves lacking many of the peaks expected across all scattering angles. Figure 1.4 shows an example of the retrieved flat phase functions from Clancy and Lee (1991) in panel a, compared to the modeled phase functions of 14 different ice crystal geometries from Yang and Liou (1996) and Yang et al. (2010) in panel b.

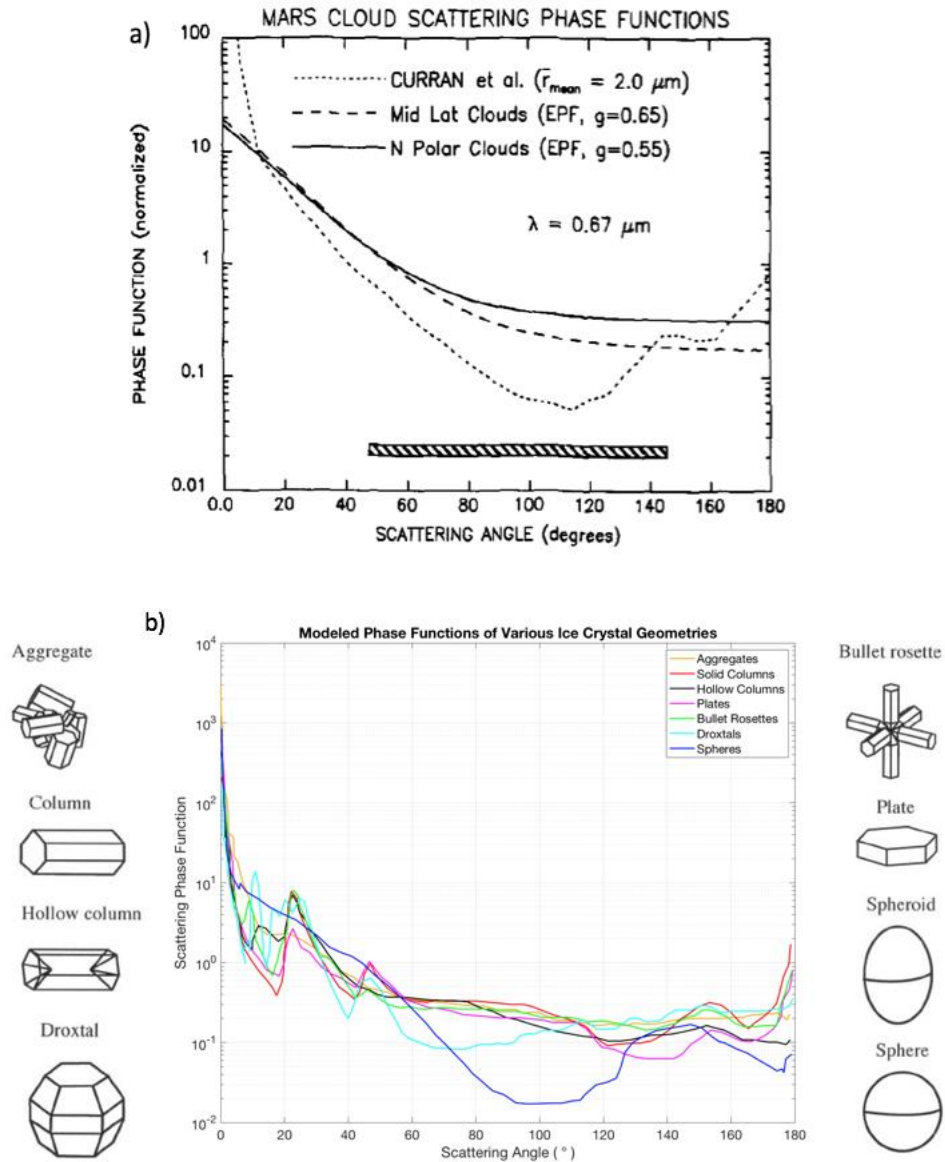


Figure 1.4: Panel a features the flat RT fit phase functions of mid latitude and northern polar latitude clouds from Viking data (Clancy and Lee, 1991) and panel b displays the modeled phase functions of seven ice crystal models and diagrams from Yang and Liou (1996) and Yang et al. (2010).

The phase functions from the ensemble models in panel b are what one would expect to see in the phase function of Martian WICs, yet the RT fit phase functions in panel a tell a different story. The peaks observed at various scattering angles in the Yang and Liou (1996) and Yang et al. (2010) phase functions are also found in similar investigations, including 9 ensemble ice crystal models from Chepfer et al. (2002). Many of those features correspond to optical scattering phenomena such as halos and parhelia, both of which are frequently observed on Earth, as seen in Figure 1.5.



*Figure 1.5 : Visual examples of some of the scattering phenomena caused by water ice crystals suspended in the Terrestrial atmosphere, that correspond to peaks in their modeled phase functions around 22°, 46° and many more (International Cloud Atlas; Atmospheric Optics).*

To help resolve this discrepancy, other WIC observations such as fall streaks can be utilized to constrain crystal size. A fall streak (also known as virga) is a form of precipitation that evaporates before it reaches the surface. Figure 1.6 displays the contour plot of a lidar detection of virga from the Phoenix lander mission in the northern Martian arctic (Whiteway et al., 2009). From the fall rate of the observed

virga, dimensions similar to those sampled in terrestrial cirrus (Whiteway et al., 2004) were approximated (42 microns x 127 microns) for a columnar ice crystal shape. Despite this, detections of optical effects at specific scattering angles commonly associated with columnar ice crystals such as pillars, halos, arcs etc., (Greenler, 1980) have yet to be confirmed on Mars regardless of the similarities in temperature and pressure to the Terrestrial stratosphere.

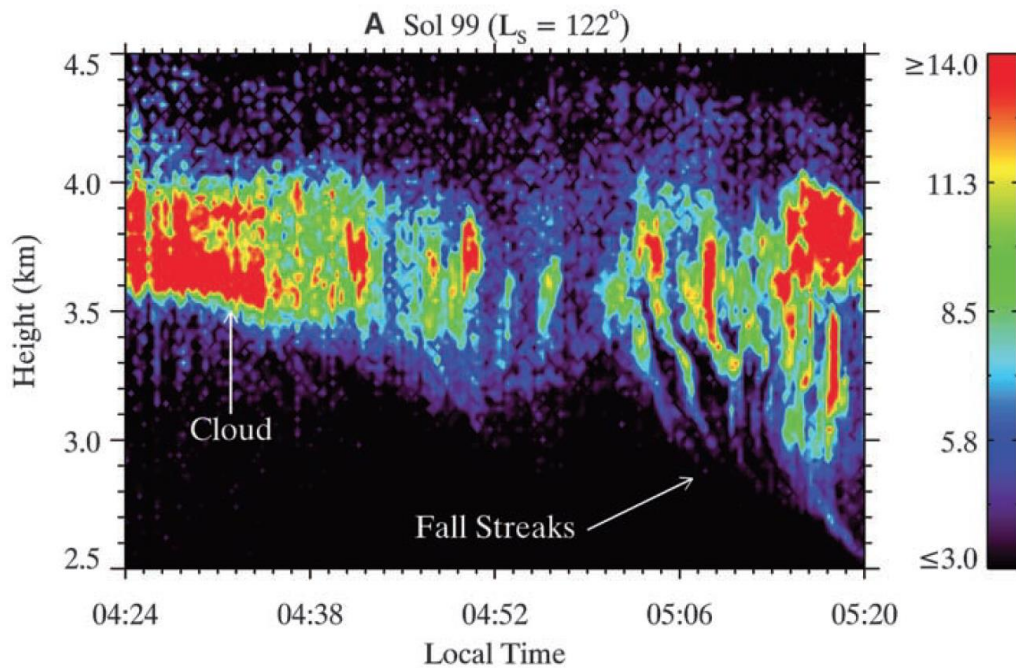


Figure 1.6: The lidar contour plot from Whiteway et al. (2009) showing the detection of Martian WICs on the left, and precipitation in the form of virga on the right. The fall streaks were consistent with columnar ice crystals 127 microns in length.

This disparity could be related to the dynamics required for various scattering phenomena; parhelia and pillars require unified orientations of hexagonal

plates and columns caused from the crystals falling through still air, while circular haloes require randomly oriented plates and columns in a more turbulent atmosphere. With that being said, at least one of those dynamical conditions should be met at any point in time, and thus it cannot be simply assumed that the ice crystal geometries dominating Martian WICs are identical to those that dominate terrestrial cirrus clouds.

While there exists one claim of a type of halo referred to as a “subsun” being observed within an MOC image (Können, 2006), it is much more likely that the observed feature in Figure 1.7 was the opposition surge, which is visible in a great number of MOC (Wang, 2002) and MARCI images. A subsun is a reflective halo caused by specular reflection off horizontally oriented ice crystal plates (Greenler, 1980), however the feature in question occurred at a point in the image where the scattering angle approached  $180^\circ$  (Wang, 2002). Können (2006) attributed the feature to a specular reflection off of hexagonal plates with a  $1^\circ$  tilt, but did not take into account the viewing geometry over the entire image. The reflection occurred at a point on Mars where from the reflector’s perspective, MOC was directly in-between the sun and the reflecting surfaces (producing the  $180^\circ$  scattering angle).

Taking MGS’s 2am-2pm sun-synchronous orbit into consideration, the common zenith angle of MOC and the Sun with respect to the location of the reflector would have been larger than the  $1^\circ$  tilt of the plates that Können (2006) calculated. Thus it would not be possible for MOC to detect a specular reflection within the scenario Können (2006) described, and is much more likely that what was observed was in fact the opposition surge.

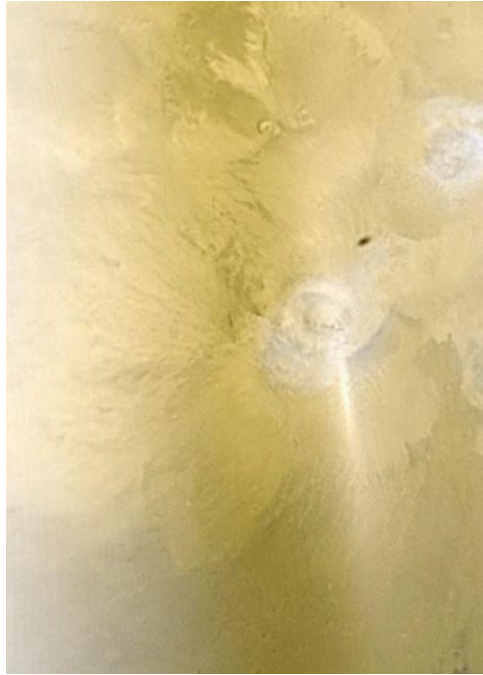


*Figure 1.7: The bright feature in this image captured by MOC was labelled a subsun by Können (2006), but given the orbit and viewing geometry of MOC at the time the image was captured, it is more likely that the feature is the opposition surge.*

The refraction and scattering processes that produce pillars and halos are directly related to the geometries of the ice crystals in the atmosphere, and their orientations (Greenler, 1980). This would lead one to conclude that if such phenomena have yet to be observed on Mars, then the geometries of the ice crystals in the Martian atmosphere differ from those commonly found on Earth.

While all scattering phenomena are dependent on scattering angle, certain features such as arcs are also dependent upon solar elevation, making them tricky or impossible to observe from orbit. When it comes to observing from the Martian

surface, even if everything else is done correctly, the added optical depth and reduced visibility from the dust suspended in the atmosphere can hinder detection of these often diffuse and faint features.

Having a better understanding of the ice crystal habit and phase function of Martian WICs would directly benefit Martian climate modelers who currently assume spherical and cylindrical particles for their models (Clancy et al., 2003, Wolff et al., 2009). Therefore, this knowledge would also benefit future work to model the role of WICs in Mars' radiation budget.

## 1.5 Constraints on the Phase Function and Ice Crystal Habits of Martian WICs

In 2016, Kloos et al. used a technique that was similar in nature to the terrestrial retrievals outlined in Chepfer et al. (2002) to constrain the general phase function of Martian WICs. That study resulted in a low resolution constraint on the lower bound of the Martian WIC phase function over a scattering angle range of  $70^{\circ}$ - $115^{\circ}$ . In order to achieve this, Kloos et al. (2016) utilized a number of single pointing cloud movies taken by the MSL navigation cameras (Navcam) at various observation times, for a little over a Martian year.

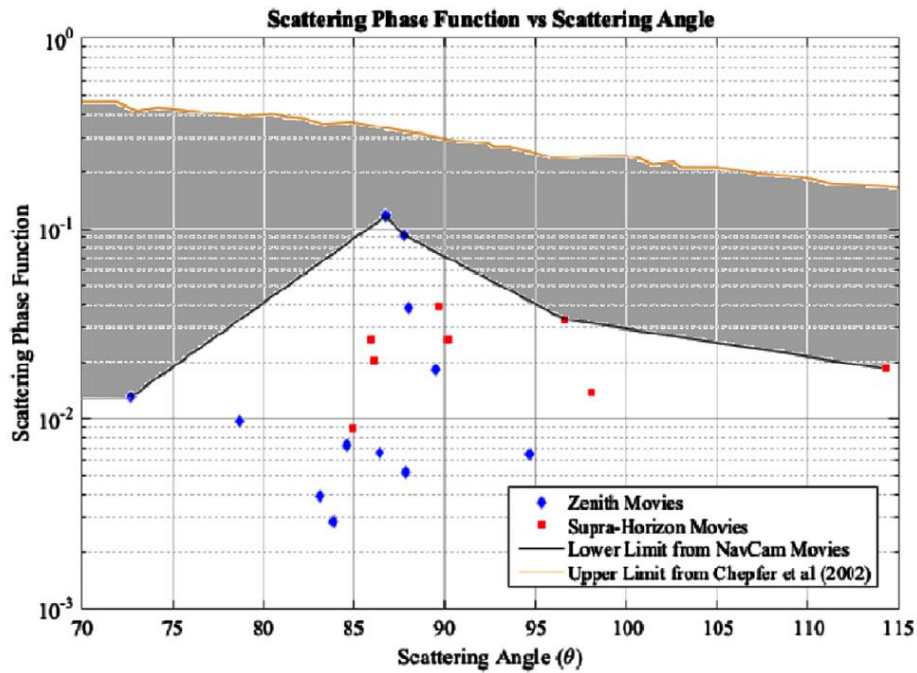


Figure 1.8: A low resolution constraint of the lower bound of the Martian WIC phase function from Kloos et al. (2016) was derived from Navcam cloud movies captured over the span of a Martian year. The upper bound of the data points from Kloos et al. (2016) act as the lower bound of the phase function in this plot because the method used to derive the data inputs for the phase function calculation produces a value that is on the lower bound of the actual value, and thus the resultant phase function also becomes a lower bound.

This thesis work improved upon the phase function investigations of Kloos et al. (2016), by determining a higher resolution constraint for the scattering phase function. The increased resolution and scattering angle range necessary for the improved phase function determination were achieved through the development of

a new Navcam activity onboard MSL specifically designed for this purpose. This new observation labeled the 'Phase Function Sky Survey' (PFSS) was implemented regularly during the ACB season to document Martian WICs at different times of day, over a wide range of scattering angles.

The resultant data was compared with previously developed composite EPF and RT modeled phase functions from Clancy and Lee (1991) and Clancy et al. (2003) along with the modeled phase functions of 7 randomly oriented ice crystal habits from Yang et al. (2010), in order to constrain dominant ice crystal geometries and the observed phase function curve for Martian WICs.

In addition to investigation of the Martian WIC phase function from the Martian surface, this work also extended its reach into Martian orbit with the analysis of publicly available MARCI image data. The extension of the phase function investigation to include data from MARCI's primary science phase (PSP) allowed for the broadening of the range of observations of clouds from a single aphelion season at one distinct location within a crater, to a globally expanded range of Martian longitudes and latitudes over two MYs, and five distinct wavelength filters. It was important to try to go beyond the MSL observations within Gale crater, as the local meteorology and dynamics within the crater produce a microclimate that is not necessarily indicative of other regions on the Martian surface at similar latitudes (Miller et al., 2018).

Once the phase functions of Martian WICs observed via MARCI were constrained, the results were compared to the phase functions from Clancy and Lee (1991), Clancy et al. (2003), the modeled phase functions of the 7 randomly oriented

ice crystal habits from Yang et al. (2010), and our MSL-derived phase functions from the surface. Additionally, the MARCI-derived phase function at  $180^\circ$  was used to appraise the use of a Terrestrial empirical relationship for deriving ice water content (IWC ) from water ice extinction or opacity from Dickinson et al. (2011) in the case of Martian WICs, and to compare the visible half-widths-half-maximums (HWHMs) of five composite MARCI images to the HWHMs modeled by Chepfer et al. (2002), Yang and Liou, (1996) and Yang et al. (2010) for water ice crystals.

## 1.6 Organization of Thesis

Chapter 2 of this thesis will discuss the MSL data and analysis methods in detail, while Chapter 3 will look at the results and discussion of the MSL dataset. Chapter 4 will cover the calibration of the MARCI dataset and the methods used to analyze the data, while Chapters 5 and 6 will discuss the results and discussion, respectively. Chapter 7 will conclude the thesis with a summary of the methods and findings of both data sets and how they can contribute to our understanding of the role that Martian WICs play in the Martian atmosphere.

# Chapter 2

## MSL Dataset and Analysis Methods

### 2.1 MSL Navcam Phase Function Sky Survey (PFSS)

The MSL Navigation Camera (Navcam) is composed of two sets of stereo cameras mounted to the rover's mast with a 200 nm spectral bandpass (600 to 850 nm) and a 45° x 45° field of view (MSL Camera Software Interface Specification, 2015, and Maki et al., 2012). It was chosen based upon the fact that clouds have been detected in Navcam data products at a relatively predictable rate since MSL landed at Gale Crater (Moores et al., 2015, Kloos et al., 2016) and that a properly exposed image has a signal to noise ratio of 200:1 (Maki et al., 2012).

The Navcam PFSS sequence was designed to be executed onboard MSL during the aphelion season, when clouds are most likely to be observed near the equator (Wolff et al., 1999). Each PFSS is composed of nine sun-relative pointings, and three images captured at each pointing to total 27 images. The nine pointings were divided into two elevation tiers for maximum coverage of the sky around the rover, as seen in Figure 2.2. Six 'lower tier' pointings had their centres at +30° elevation above the local level (LL) horizon and were separated by 48° in azimuth, and the three remaining 'upper tier' pointings had their centres at +70° LL elevation with 120° separation in azimuth.

### Phase Function Sky Survey Image Pointing Projections

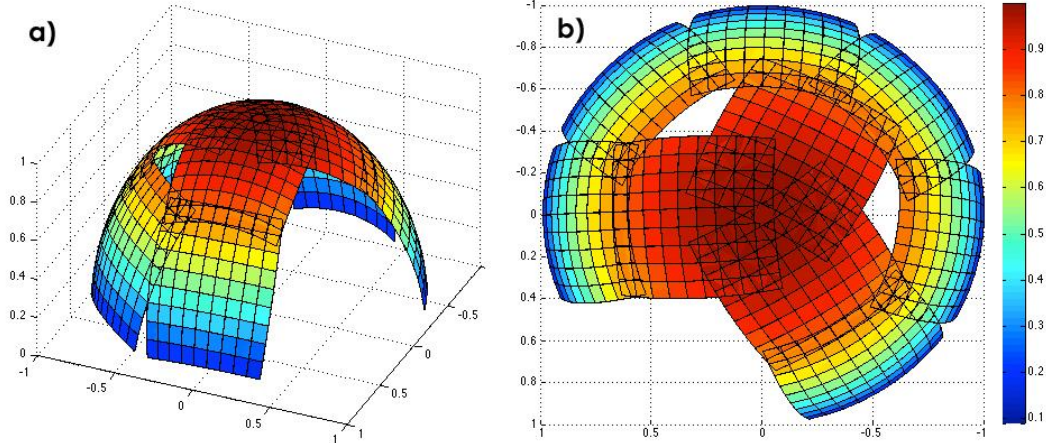


*Figure 2.1: Projections of PFSS frame pointings on a dome, with MSL assumed to be at the centre. The gap in the pattern prevents the NavCam from pointing close to the sun where the variation in radiance over the frame exceeds the 200:1 SNR of the imager. The colour represents the cosine of the zenith angle.*

The gap shown at lower right in panel a and lower left in panel b of Figure 2.1 was intentionally pointed towards the sun and to avoid exposing other science instruments to a prolonged sun pointing. The sequence was modified as part of the tactical planning process to accommodate a range of morning and evening observations to investigate diurnal variations in Martian WICs through their phase functions. An example mosaic from a single PFSS observation is shown in Figure 2.2 for reference.

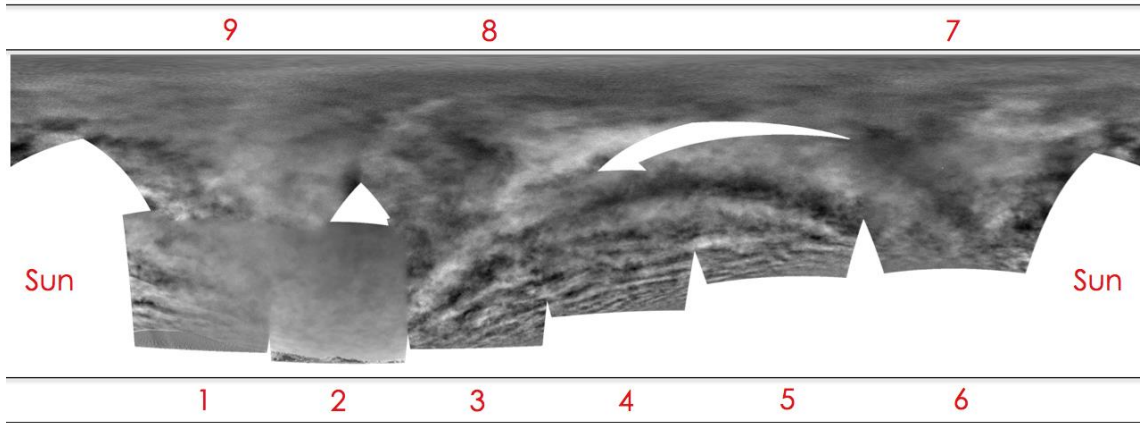


*Figure 2.2: An example of the two tiers of PFSS frames at each of the nine observation pointings. In this particular observation taken on Sol 1924 at 07:05 local true solar time (LTST), the frames corresponding to pointings 1 and 2 contained surface features causing the rover's onboard auto exposure algorithm to expose for the foreground, resulting in a lightened appearance. Frames 4, 5, and 6 had increased elevations to avoid larger surface features, and were further amplified by the tilt of the rover at the time of image capture. Cloud features resembling gravity waves were observed from horizon to horizon in this early morning observation.*

The desired cadence for the PFSS was to obtain two observations within the span of 14 Martian sols, and 50% of the total observations should occur before noon and the remaining 50% after noon, within the time constraints previously mentioned. This cadence only existed for the areocentric  $L_s$  range of  $50^\circ$  to  $150^\circ$ , or until clouds were no longer consistently observed. This range was determined based on Figure 6 from Kloos et al. (2018).

## 2.2 Deriving the Phase Function from MSL Navcam Imagery

In the context of this work, the phase function,  $P(\cos \Theta)$ , is a non-dimensional parameter that describes the angular distribution of scattered radiation by WICs, as a function of scattering angle. The phase function describes the scattering properties of individual aerosols or collections of aerosols, and is normalized by definition (e.g. Equation 3.3.10 Liou, 2002). When considering radiative transfer, the phase function enters through the source term of the radiative transfer equation, given as Equation 3.4.5 in Liou (2002):

$$\mu \frac{dI(\tau, \mu, \varphi)}{d\tau} = I(\tau, \mu, \varphi) - J(\tau, \mu, \varphi) \quad (2.1)$$

Here  $I(\tau, \mu, \varphi)$  is taken to be the upward radiance from the atmosphere or WIC, and  $J(\tau, \mu, \varphi)$  is the source term. Both are functions of optical depth  $\tau$ , the cosine of the emission zenith angle  $\mu$ , and the azimuthal angle  $\varphi$ . The geometry described by Equation 2.1 can be seen graphically in Figure 2.3. The increase in radiance as radiation propagates is represented by the source term, and as the main source of the radiation being considered is solar radiation scattered off optically thin WICs (such as those observed from the surface of Mars in Moores et al., 2015 and Kloos et al., 2016), a single scattering approximation will be used. The single-scattering assumption can be further justified by the fact that scattering from the dust in the atmosphere, and diffuse upward reflectivity from the surface ( $\sim 25\%$  of the downward flux within the Navcam bandpass; Johnson et al., 2003), is uniform across an image and thus disappears with implementation of the mean frame

subtraction technique outlined later in this section. The source term may be approximated as:

$$J(\tau, \mu, \varphi) \cong \frac{\omega}{4\pi} FP(\Theta)e^{\frac{-\tau}{\mu_0}} \quad (2.2)$$

The core parameters of this term are optical depth  $\tau$ , phase function  $P(\Theta)$ , and a single scattering albedo  $\omega$  equal to 1 for Martian WICs (Clancy et al., 2003). Equation 2.2 (Equation 3.4.10 from Liou, 2002) denotes the adopted WIC source term where  $F$  is the flux at the cloud,  $P(\Theta)$  is the single scattering phase function dependent on scattering angle  $\Theta$ , and  $e^{\frac{-\tau}{\mu_0}}$  is the transmittance through the atmosphere to the location of the cloud.

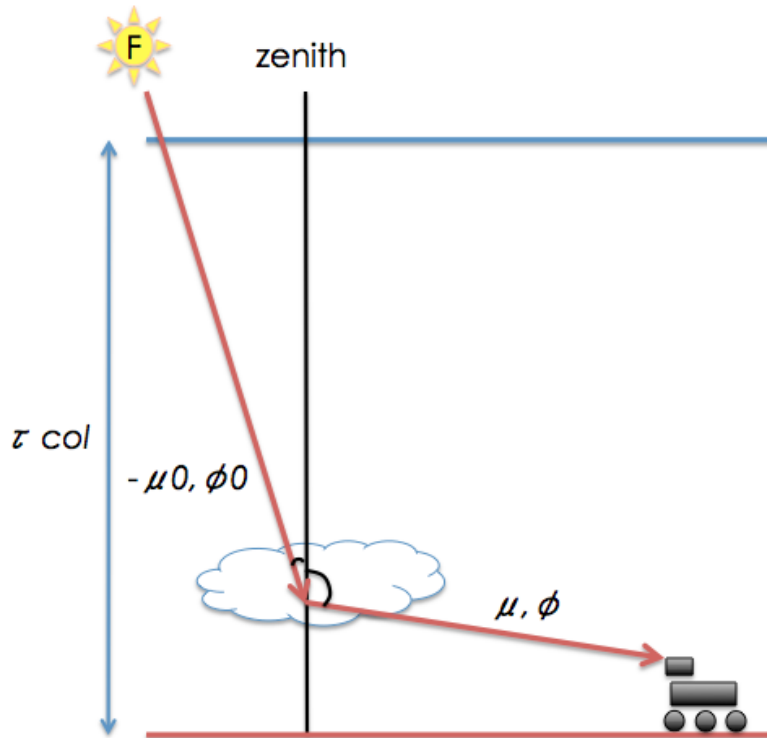


Figure 2.3: A visual representation of the phase function redirecting incident radiation  $I(F)$  from  $(-\mu_0, \varphi_0)$  at the top of the Martian atmosphere to  $(\mu, \varphi)$  after scattering off water ice crystals in a cloud (note:  $-\mu_0$  is equal to  $-\cos(\theta_0)$ ,  $\mu$  is equal to  $\cos(\theta)$ ),

and  $\theta_0, \theta$  are the corresponding zenith angles). The angle between  $(-\theta_0, \varphi_0)$  and  $(\theta, \varphi)$  is denoted the phase angle, and the scattering angle  $\Theta$  is therefore equal to  $(\pi - \text{phase angle})$ ; simply the angle that radiation was scattered from its incident trajectory. During the process depicted, the radiation is attenuated through an optical depth of atmosphere  $\frac{\tau_{col}}{\mu_0}$  before scattering off a cloud toward Navcam.

As most of the clouds observed in the ACB are assumed to be located at several scale heights above the surface based on MCS retrievals (Kloos et al., 2016; Moores et al., 2015; Kleinböhl et al., 2009), it is reasonable to assume that most atmospheric dust lies between Navcam and the cloud, and that no additional scattering exists above the cloud. The downward scattered light intensity is reduced to the cloud's source term integrated over its optical depth. Adopting the assumptions outlined by Kloos et al. (2016), the downward scattered light radiance originating from a cloud is reduced to Equation 2.3, where  $\Delta\tau$  is the integrated optical depth of the cloud (Equation 6 from Kloos et al., 2016):

$$I(\Delta\tau, \mu, \varphi) = \frac{\Delta\tau}{4\pi\mu} FP(\Theta) \quad (2.3)$$

This equation does not include the intervening dust between the Navcam and the cloud. To take the dust into account we use measurements of optical depth,  $\tau_{col}$ , made by MSL's Mast Camera (Mastcam) (Lemmon et al., 2016 and Vasavada et al., 2017), with average uncertainties of 10%, adjusted for the viewing angle. The lowest elevation angle in an image was  $7.3^\circ$ , making the plane-parallel

approximation  $\tau_{col}/\mu$  valid for the observed range of Mastcam column optical depths of 0.224-0.587, giving the highest possible path optical depth of 4.6.

Finally, we restrict the measurement to the width of the camera band-pass of 250 nm (Maki et al., 2015). Equation 2.3, which gave the downward radiance of WICs, is altered with the addition of these parameters to produce the resultant radiance observed at the imager (Kloos et al., 2016):

$$I_{\lambda,VAR}\Delta\lambda = \frac{\Delta\tau}{4\pi\mu} FP(\Theta) e^{-\frac{\tau_{col}}{\mu}} \quad (2.4)$$

Equation 2.4 (Equation 10 in Kloos et al., 2016), gives the varying radiance,  $I_{\lambda,VAR}\Delta\lambda$ , from the WICs observed in a PFSS.

In order to isolate the downward spectral radiance  $I_{\lambda,VAR}$  of the cloud from the PFSS data, a mean frame subtraction (MFS) technique was used to remove the constant radiance of the atmosphere, isolating the radiance that varied due to the motion of WICs. This technique has been previously used on Phoenix (Moores et al., 2010) and MSL (Moores et al., 2015) data. At least three images are acquired at each observation pointing to allow for a mean frame to be created, and that resultant mean frame is then subtracted from the images used to create it.  $I_{\lambda,VAR}$  is then calculated by differencing adjacent regions of comparatively high and low spectral radiance (as seen in Figure 2.4). The region with low spectral radiance is assumed to be completely cloud-free, thus  $I_{\lambda,VAR}$  is considered a lower bound on the spectral radiance of the cloud.

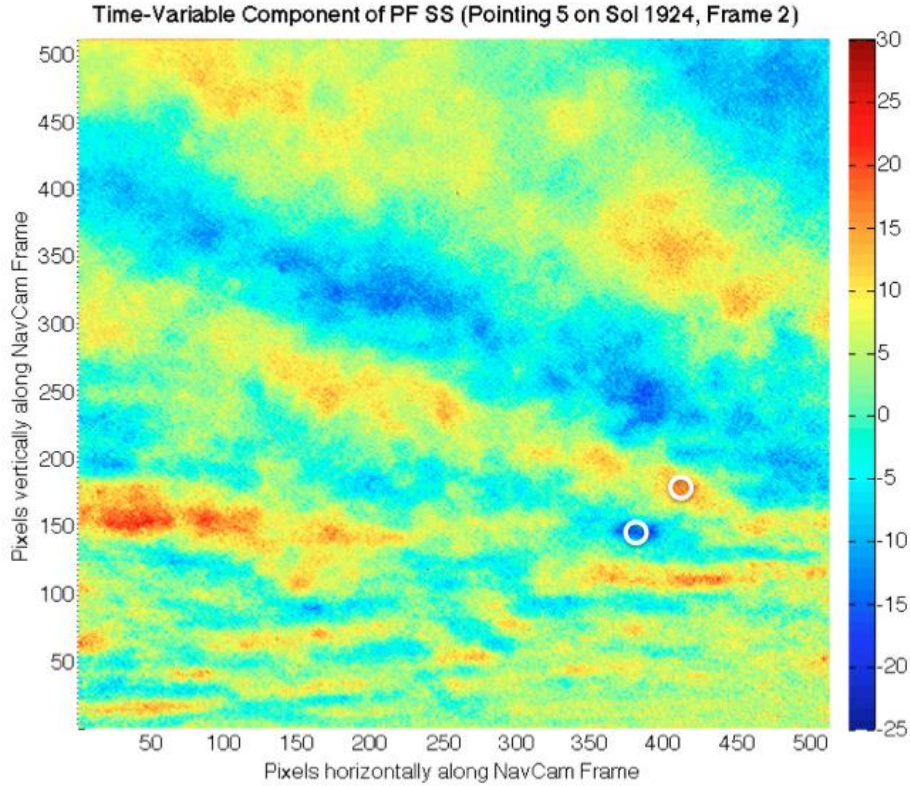


*Figure 2.4: An example of the MFS time-variable component used to calculate one instance of variation in spectral radiance in a PFSS run executed on Sol 1924. The outlined regions are just one example of a region that could be used to calculate the variation in spectral radiance within this image. The second MFS frame from each of the 9 pointings was chosen to isolate this variable.*

Two regions were selected from the middle perturbation frame of each of the 9 pointings in every phase function observation for the determination of  $I_{\lambda,VAR}$ . The exact location of the cloud in the image was used to calculate the scattering angle for the subsequent phase function derivation. Equation 2.5 was then used to solve for the phase function once values for  $I_{\lambda,VAR}$  were derived from the MFS of the PFSS data. The integrated cloud optical depths used were derived from MCS integrated

cloud optical depths with uncertainties ranging from 0.1% to 10%, averaged over the last three MYs within a  $5^\circ$   $L_s$  range from the  $L_s$  of each PFSS observation. They were normalized from thermal infrared to 880 nm for Navcam by a factor of 3.6 (Guzewich et al., 2017, Kleinböhl et al., 2011 and 2017, and Montabone et al., 2015). The use of MCS optical depths provides a way to uniquely determine the phase function as the radiance observed by Navcam is a function of both the phase function, i.e. how much light is scattered into the solid angle that the camera can observe, and how much material there is to scatter light. In previous work, such as Kloos et al (2016; 2018) an assumed value of the phase function was used to calculate optical depth. Rearranging Equation 2.4 using this information yields:

$$P(\Theta) = \frac{4\pi\mu I_{\lambda,VAR}\Delta\lambda}{\Delta\tau_{MCS}F_{\lambda}e^{-\frac{\tau_{col}}{\mu}}} \quad (2.5)$$

Note that in Equation 2.5 spectral irradiance,  $F_{\lambda}$ , is integrated over  $\Delta\lambda$  from the extraterrestrial spectrum provided in the ASTM G-173 model (ASTM International, 2012), adjusted for Mars' distance from the Sun corresponding to each observation. The labels of the data files also provided the pertinent information regarding image pointings to determine the viewing zenith angles for each pixel, as well as the corresponding scattering angles for phase function analysis.

Taking into account the upper bound of uncertainty for MCS optical depths of 10%, and the average uncertainty for Mastcam column optical depths of 10%, the phase function values retrieved from Equation 2.5 would have an uncertainty with an upper limit of approximately 12%. This was determined using a linear approximation for the uncertainty of the  $e^{-\frac{\tau_{col}}{\mu}}$  term, with the minimum Mastcam

column optical depth of 0.224 and lowest elevation angle of  $7.3^\circ$ , to maximize the uncertainty term. It should also be noted that the calculation of the phase function is relatively insensitive to the 3.6 factor used to normalize the MCS optical depths, as it only lowers the magnitude of the curve uniformly at each scattering angle, and doesn't change the shape. The effects of this factor are essentially removed when the phase function is normalized.

The final step in deriving the phase function curve is typically to normalize the results over all scattering angles from  $0^\circ$ - $180^\circ$ . Unfortunately, it was not geometrically possible for the PFSS to observe over that entire range, making it impossible for the resultant phase function to be normalized without reference to previous work. However, as the shape of the phase function is more relevant than the absolute magnitude for analysis, our results were normalized by the average value of the TES-derived aphelion WIC phase functions (Clancy et al., 2003) at the median observed scattering angle.

# Chapter 3

## MSL Dataset Results and Analysis

### 3.1 MSL Navcam Phase Function Sky Survey Results

The PFSS sequence was executed 35 times in the MY 34 aphelion season, over  $L_s$  range of  $61.9^\circ$ - $156.5^\circ$ . Figure 3.1 displays the temporal distribution of these PFSS runs. 20 occurred in the morning hours between 06:00 and 09:30 LTST, and 15 runs occurred in the evening hours between 14:30 and 18:00 LTST, with an operationally required 2.5 hour gap on either side of local noon due the sun being located near zenith.

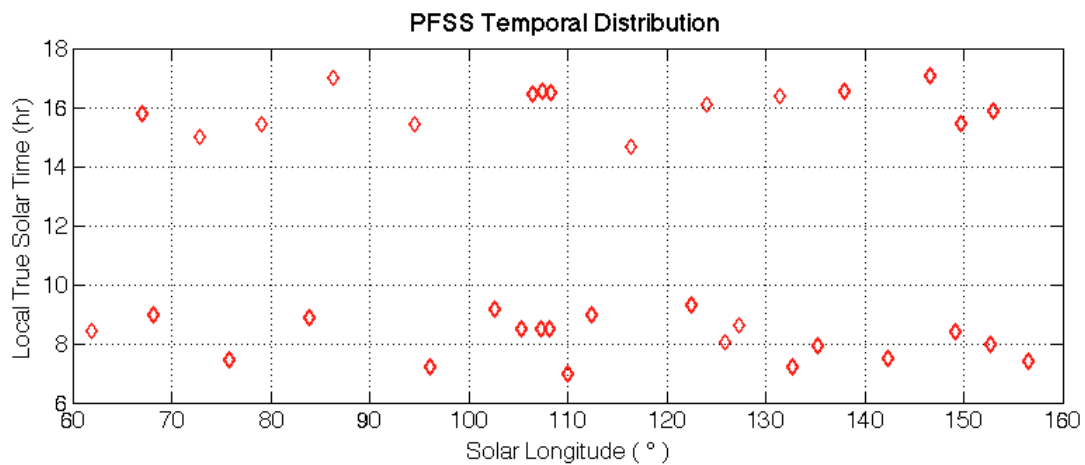
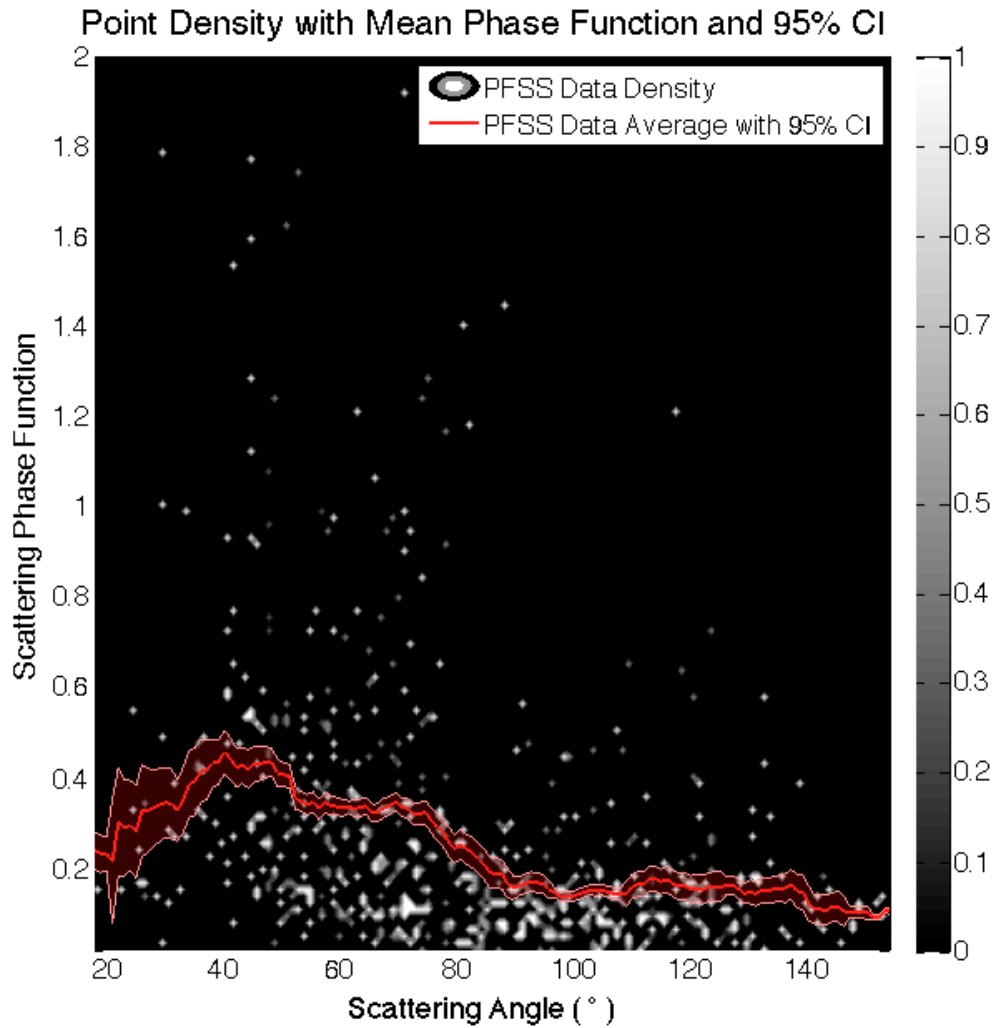


Figure 3.1: The temporal distribution of the 35 PFSS runs is displayed with respect to LTST and  $L_s$ . The observation was run over as many varying LTST's as possible (given

*the MSL engineering and useable data constraints) in an attempt to reduce diurnal data bias.*

The phase function was derived from the PFSS data using the method outlined in Chapter 2. Compared to the previous work of Kloos et al. (2016), the number of data points available to derive the phase function grew from 20 to 630, in this work, and the normalized magnitudes of the phase function ranged from 0.0016 to 2.1, spanning scattering angles  $18.26^\circ$  to  $152.56^\circ$ . The data was binned by two dimensions into 137 phase function and 137 scattering angle bins, and then a mean phase function curve was produced by using a rectangular sliding average with a 15 bin window to reduce the 95% confidence interval to an average of 10% of the phase function. The combination of retaining a large number of bins and applying a sliding average was adopted to produce curves with reduced noise for the mean of the phase function, whilst preserving small yet potentially important scattering features. As the value obtained for  $I_{\lambda,VAR}$  is assumed to be on the lower bound of the expected value, the resultant phase function is also assumed to be a lower bound. The resultant curve and 95% confidence interval of the sliding average window centered on each point, are displayed graphically in Figure 3.2.



*Figure 3.2: The mean curve of the derived phase function data binned by scattering angle and phase function is displayed overtop of the data point density with shaded error bars corresponding to the 95% confidence interval of the sliding average window centered on each point. The data density was calculated by dividing each two dimensional bin by the total number of data points in its respective scattering angle bin.*

In Figure 3.2, the 95% confidence interval varies along the curve as a result of the range of data points in the sliding average window, centered on each point. The mean derived phase function has local maxima around the 22°, 46°, and 70° scattering angles that are allowed, but not required. Local minima observed around scattering angles of 50°, 100° and 140° are also allowed but not required. To test whether the mean phase function was distinguishable from a featureless curve, a null hypothesis of  $phase\ function = 0.55 \times e^{\left(\frac{scattering\ angle - 40^\circ}{50^\circ}\right)}$  was used, and a chi-squared p-test was implemented. The resultant weighted chi-squared value was 0.48, and the p-value was greater than or equal to 0.49, and therefore not statistically significant for rejection of the null hypothesis.

## 3.2 Comparison to PFs of Known Ice Crystal Geometries

In Figure 3.3, our derived phase function was compared with seven randomly oriented and isolated ice crystal geometries from Yang and Liou (1996), and Yang et al. (2010); spheres, hexagonal plates, droxtals, aggregates, bullet rosettes, and hexagonal solid and hollow columns. This analysis simply constrained the dominant ice crystal habit over the entire period of observation, including observations from all times of day.

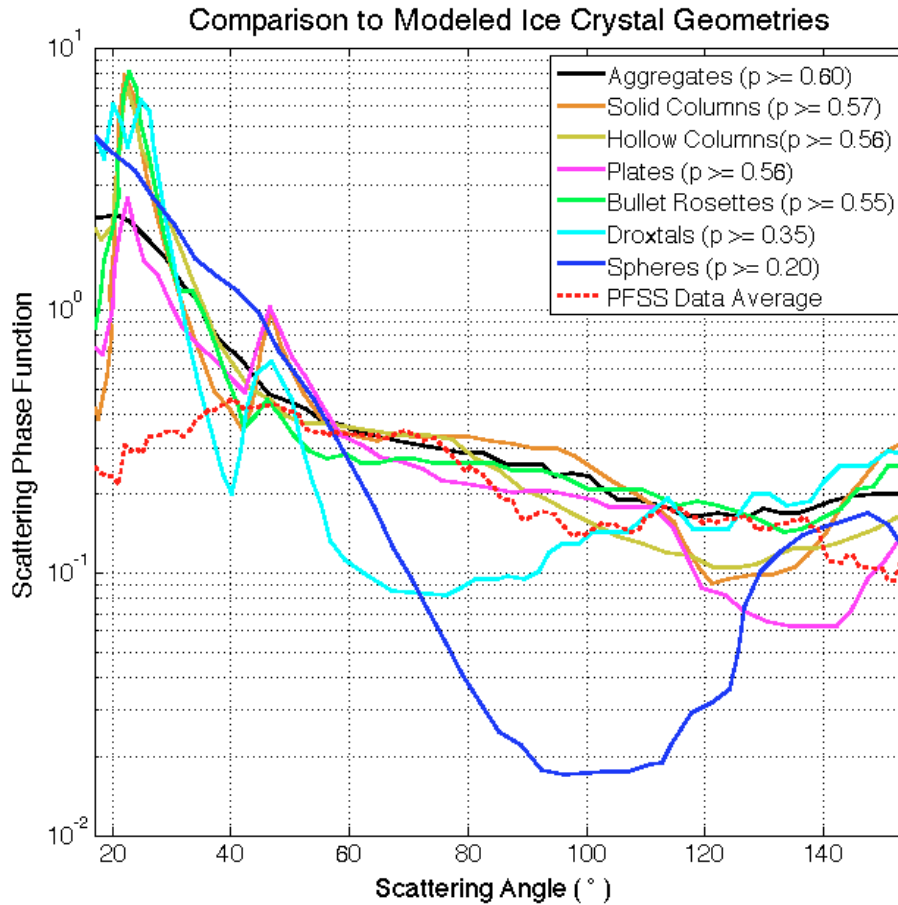


Figure 3.3: The normalized mean curve of our results, along with the 7 modeled phase functions for various ice crystal geometries from Yang and Liou (1996), and Yang et al. (2010) extracted using WebPlotDigitizer (Rohatgi, 2018). The PFSS data was normalized at the median scattering angle bin,  $85^\circ$ , to the average phase function value in Clancy et al. (2003) for type 1 and 2 aphelion WICs. A weighted chi-squared test was run and the probabilities of fit for the phase function data with respect to the modeled curves are given in the legend as  $p$ -values, with aggregates being the most probable and spheres being the least.

A weighted chi-squared analysis with a p-test and residuals analysis was used to compare the goodness of fit of the phase function data with each of the randomly oriented modeled ice crystal geometries from Yang and Liou (1996), and Yang et al. (2010). The resultant p-values listed in the legend of Figure 3.3 show that the WICs we observed have the highest probability of containing aggregates, with a weighted chi squared value of 0.27, and a p-value greater than or equal to 0.60. Only slightly less probable, were solid hexagonal columns with a weighted chi squared value of 0.33 and a p-value greater than or equal to 0.59, and hexagonal hollow columns and plates with weighted chi squared values of 0.34 and p-values greater than or equal to 0.56. Bullet rosettes had a weighted chi squared value of 0.36, and a p-value greater than or equal to 0.53. These results agree with the ice crystal habits required to produce phenomena such as the 22° halo or parhelia, and the 44° parhelia, 46° halo, or supralateral arcs, which align with the allowed local maxima at the ~22° and ~46° scattering angles in our derived mean phase function curve. The mean phase function magnitudes at these scattering angles are a great deal smaller than those modeled, suggesting that the features corresponding to those phase function peaks may not be visible on Mars. An investigation with an instrument that could allow more frequent observations at smaller scattering angles could help confirm these results, allowing us to say for certain whether these features can be observed on Mars. Halos are commonly observed in cirrus clouds composed of randomly oriented hexagonal columns and plates, while parhelia require them to be uniformly oriented. Arcs generally are formed by hexagonal columns and are not only dependent upon their orientation, but the elevation of the Sun.

The droxtal and spherical models had weighted chi-squared values of 0.87 and 1.7, and p-values of greater than or equal to 0.35, and 0.20, respectively. These probabilities are lower than the other five modeled ice crystals by a factor of about two, but they are still not statistically significant enough to be rejected as null hypotheses. Optical phenomena formed by spherical ice crystal geometries (such as rainbows, fogbows, glories, or coronae) are therefore less likely to be observed than halos, parhelia, and arcs.

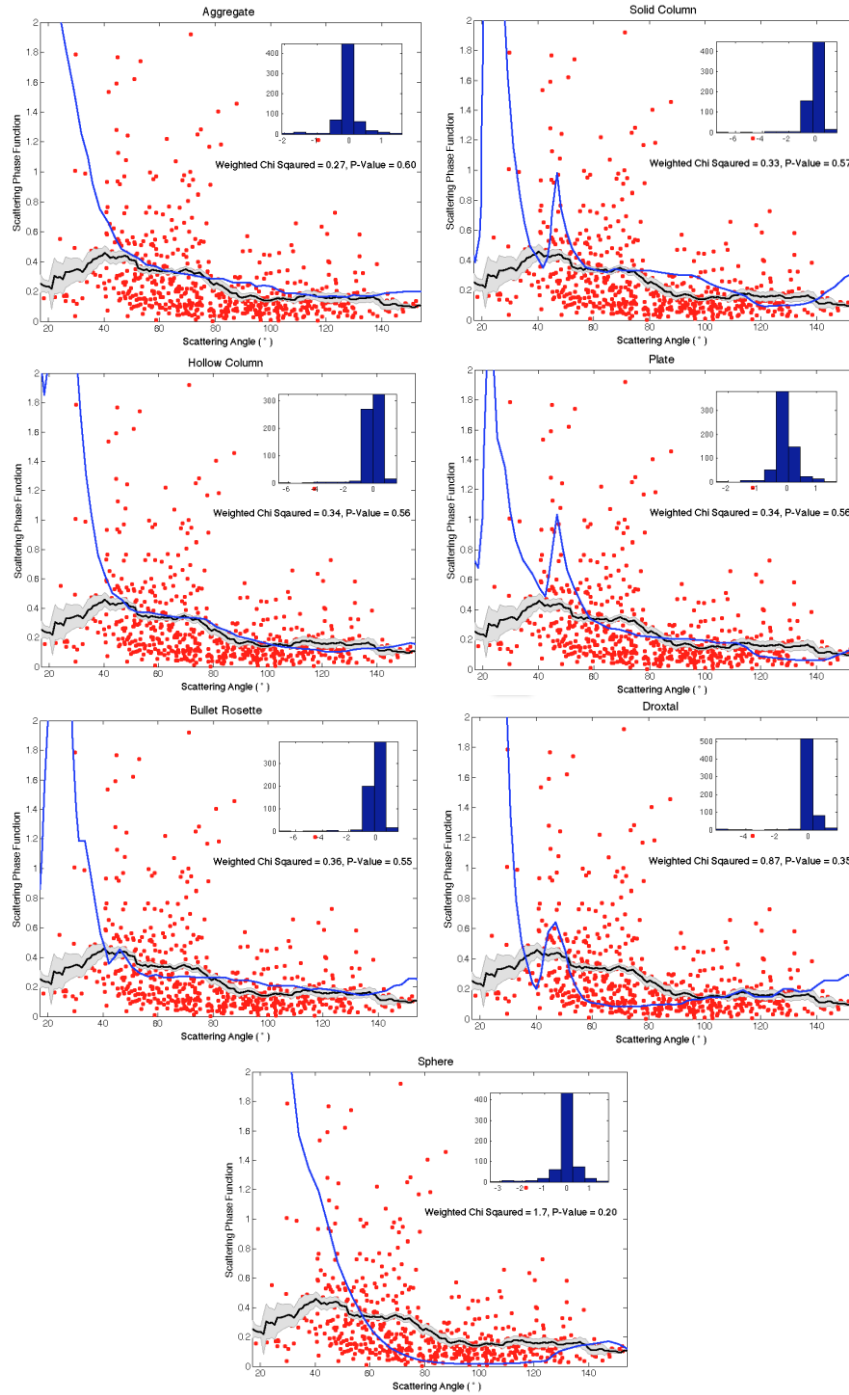


Figure 3.4: Histograms of the residuals from the phase function data and the 7 modeled phase functions for various ice crystal geometries from Yang and Liou (1996), and Yang et al. (2010), are inset in each plot. The normalized PFSS data points are

*shown with the red circles, the blue curve represents the modeled ice crystal habit being looked at within each plot, and the black curve and shaded error bar represents our mean phase function curve and 95% confidence interval of the sliding average window centered on each point. The results of the weighted chi-squared analysis and p-values for each plot are included for reference.*

Given the results of the chi-squared tests, p-tests, and residuals analysis displayed in Figures 3.3 and 3.4, the ice crystal geometries more likely to dominate WICs in the aphelion season were determined. Aggregates, hexagonal solid columns, hollow columns, plates, and bullet rosettes were found to more probably make up the Martian WIC's than droxtals or spheres, however no model was able to be rejected statistically. The hexagonal nature of the rosettes, columns, and plates also aligns with the results of an investigation confirming the physical detection of the backscatter peak from randomly oriented hexagonal water ice crystals (Zhou and Yang, 2015), and observed 180° backscatter peaks present in MARCI and MOC images (Wang, 2002). Furthermore, when Whiteway et al. sampled the shapes of ice crystals in a terrestrial cirrus cloud in 2004, they found various combinations of aggregates, hexagonal columns, bullet rosettes, and irregular crystals. Bullet rosettes appeared only at the top of the cloud, while aggregates, columns, and irregularly shaped crystals were found throughout. This agrees with bullet rosettes having a slightly lower probability of being contained within the observed WICs than aggregates, columns, or plates. It was hypothesized by Whiteway et al. (2004) that the blunt irregular crystals found to dominate the lower regions of the cirrus

were actually other crystal geometries in various stages of sublimation. As all five of the most probable geometries dominating the phase function observations have been directly observed within a terrestrial cirrus cloud, it would be reasonable to argue that irregular ice crystals could also be found in Martian WICs, especially because virga and sublimation of ice crystals has been observed on Mars (Whiteway et al., 2011). Moreover, as Whiteway et al. (2004) found 86% of the lower portion of a cirrus cloud to be composed entirely of blunt irregular crystals, it would follow that these could be a large contributor to the deviations in the observed phase function from the other modeled phase functions.

### 3.3 Comparison to Other Phase Functions for Martian WICs

Next, our derived curves were compared with previously derived and currently implemented Martian WIC phase functions from Viking (Clancy and Lee, 1991) and TES data (Clancy et al., 2003), as seen in Figures 3.5 and 3.6. In both of these publications, the phase functions were produced from the best fit of an RT model to an observationally derived EPF. The phase functions from Clancy and Lee (1991) are flat and smooth without a  $180^\circ$  backscatter peak, while the bi-modal phase functions from Clancy et al (2003) feature greater magnitude variation and hint at some of the features observed in the modeled geometries discussed in Section 3.2.

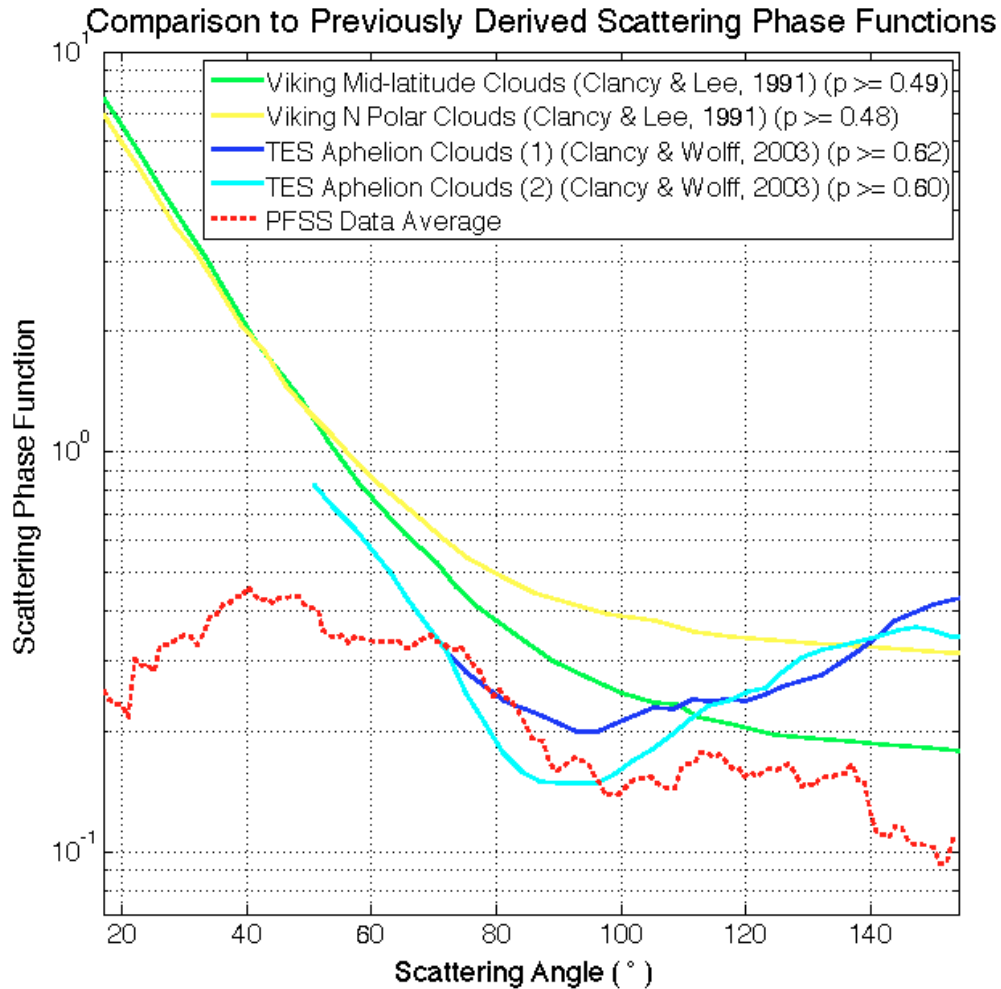
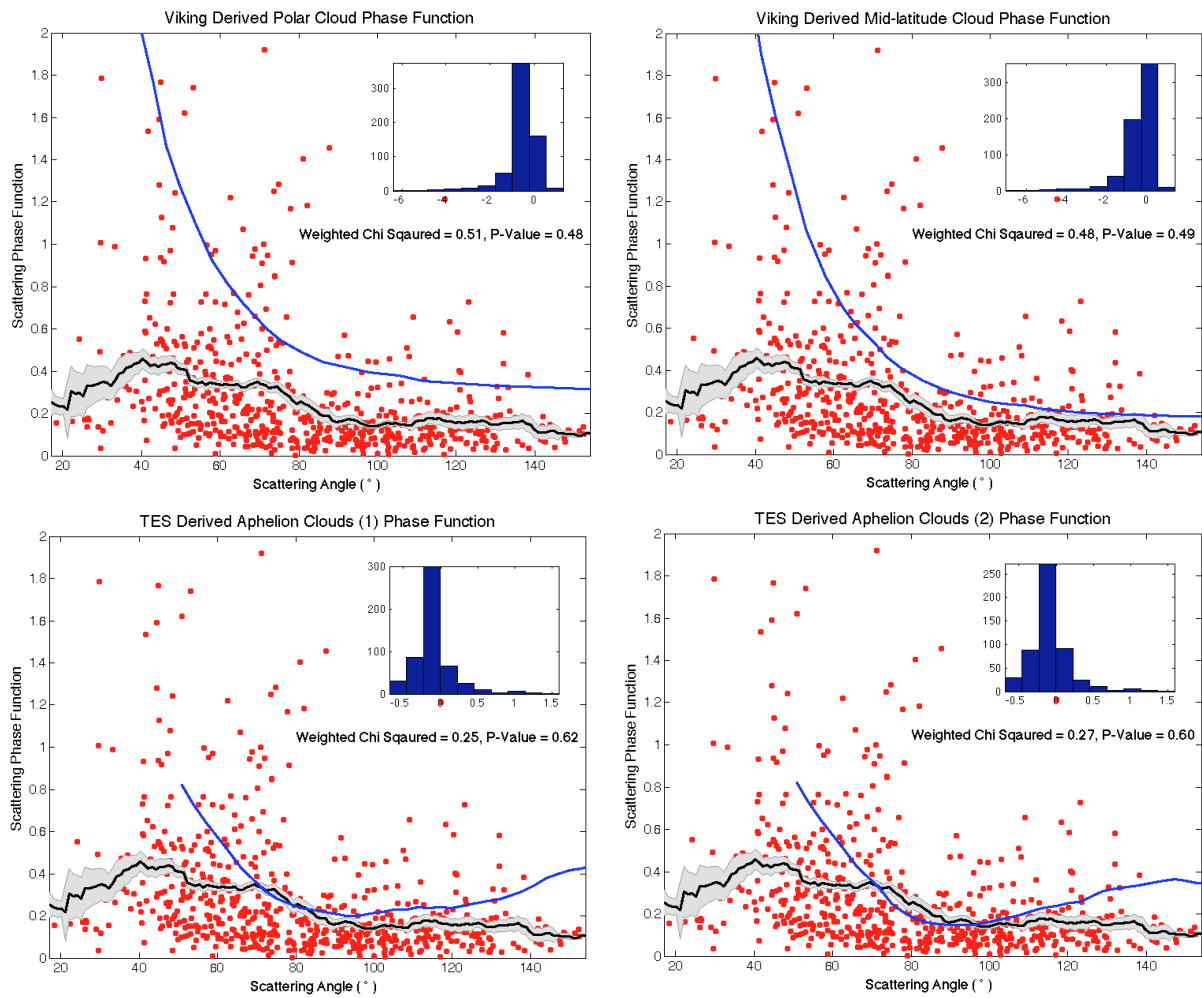


Figure 3.5: The mean and upper bound of our normalized results alongside composite RT model and EPF derived phase functions for Martian water ice clouds from Viking and TES data extracted using WebPlotDigitizer (Rohatgi, 2018). The smooth curves produced in Clancy et al. (2003) and Clancy and Lee (1991) involved the fit of RT models to EPFs captured over a finite range of scattering angles. The probabilities from a chi-squared analysis between the phase function data and EPF derived phase functions are listed beside each of the curves, with TES aphelion clouds (1) having the highest  $p$ -value, and the Viking Polar clouds having the lowest value.

Clancy et al (2003) speculated from their results that the dominant habits took the form of a spheroidal geometry for their aphelion ice aerosol. As our resultant phase function was normalized to the average phase function value of the median scattering angle for two size parameters of the aphelion ice aerosols, the results from a chi-squared goodness-of-fit analysis were weighted chi-squared values equal to 0.25 and 0.27, and p-values greater than or equal to 0.62 and 0.60, over the range of scattering angles for which they were derived.



*Figure 3.6: Histograms of the residuals from the phase function data and the four EPF derived phase functions from Viking (Clancy and Lee, 1991) and TES (Clancy et al., 2003) are inset in each plot within the figure. In each plot, the normalized PFSS data points are shown with the red circles, the blue curve represents the EPF derived phase function, and the black curve and shaded error bar represents our mean phase function curve and 95% confidence interval of the sliding average window centered on each point. The results of the weighted chi-squared analysis and p-values for each plot are included for reference.*

The Martian WIC phase functions from Clancy and Lee (1991) are flat and smooth providing very little information about source scatterers. Potential contamination from dust, or reduced formation of WICs could be two possible reasons why the phase functions derived from Viking observations may look the way they do. The Viking data was acquired over a period that we now know to have been unseasonably warm and dusty, featuring two all-encompassing global dust storms (Tamppari et al., 2000). The WIC phase functions derived in Clancy and Lee (1991) greatly resemble the dust phase functions also derived from their Viking observations, and while it was noted in Clancy et al. (2003) that the TES results for the dust phase function were consistent with those from Viking, the WIC phase functions were not. From the chi-squared probability analysis, the resultant weighted chi-squared values and p-values were 0.51, and 0.49 for the mid-latitude clouds, and 0.48, and 0.49 for the polar clouds. Lower probabilities for the Viking curves (relative to the TES curves) is expected based upon the above analysis,

however the p-values still remain greater than those for the modeled phase functions for droxtals or spheres from Yang and Liou (1996), and Yang et al. (2010).

### 3.4 Cloud Features

A qualitative analysis of the PFSS perturbation images showed that cloud morphologies agreed with those identified in previous investigations of Martian WICs. Features consistent with gravity waves (Kloos et al., 2018), ripples or a “zig-zag” pattern (Moores et al., 2010), fractus or ragged edges (Lemmon et al., 2014), and multiple cloud layers (Kloos et al., 2016) are depicted in Figure 3.7.

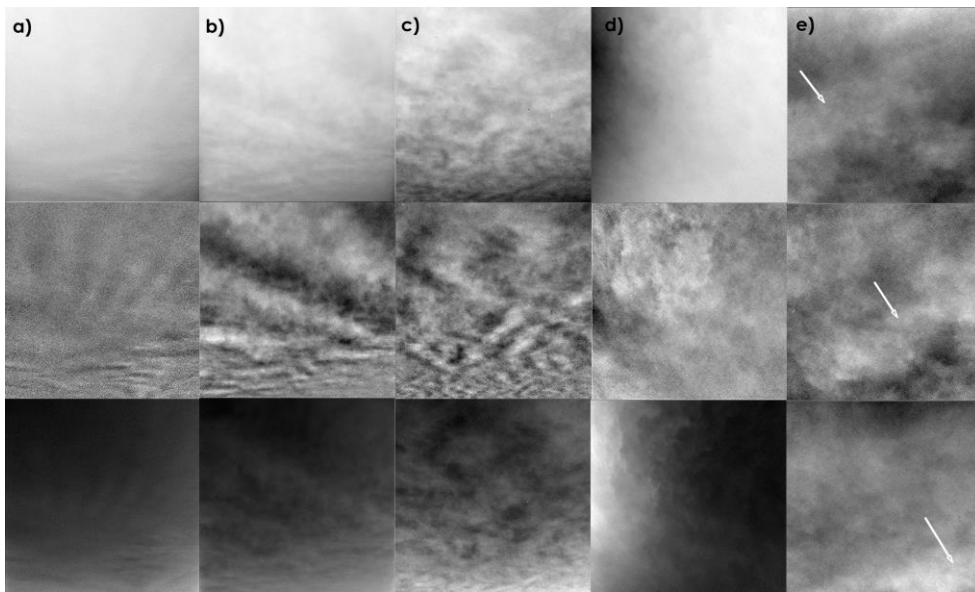


*Figure 3.7: The vertical panels show the perturbation images from a single pointing in a PFSS observation; panel a displays two faint separate cloud layers captured on sol 1849 at Ls 75.8°, panel b shows a cloud formation consistent with gravity waves taken on sol 1924 at Ls 110°, panel c displays a zig-zag or rippled cloud pattern observed on*

*sol 1971 at Ls 132.7°, panel d shows clouds with a fractus or ragged appearance captured on sol 1998 at Ls 146.6°, and finally panel e displays the movement of an optically thick feature between frames observed on sol 1968 at Ls 131.4°.*

WIC morphologies that involve parallel bands of increased spectral radiance moving equal distances across consecutive frames (such as those seen in panels a, b, and c) can be associated with layers or sheets of clouds at constant altitudes (Moore et al., 2015). In contrast, regions with infrequent wave structures and ragged edges (similar to those shown in panels d, and e) are more likely to have resulted from isolated condensates (Lemmon et al., 2014).

# Chapter 4

## MARCI Data Calibration and Methods

### 4.1 Radiometric Calibration

MARCI was launched aboard the Mars Reconnaissance Orbiter (MRO) which entered its Primary Science Phase in orbit around Mars in November of 2006. The PSP lasted until November 2008, spanning MY 28  $\sim L_s=128^\circ$  to MY 29  $\sim L_s=165^\circ$ . This study analysed publicly available raw MARCI data (dataset ID: MRO-M-MARCI-2-EDR-L0-V1.0; Malin et al., 2001) downloaded from the Planetary Data System (PDS; Eliason et al., 1996), captured during the aphelion seasons ( $\sim L_s=42^\circ$ - $170^\circ$ ) within the PSP. The boundaries of the solar longitude range of interest were selected based upon the results of the Kloos et al. (2018) analysis of ACB cloud optical depths as observed from MSL.

During the PSP, MRO was typically in a 3am-3pm sun-synchronous orbit (Figure 4.1 panel a) that allowed MARCI to capture 12 to 13 images per sol in five visible and two ultraviolet wavelength filters (Zurek and Smrekar, 2007). These filters were permanently mounted on top of MARCI's  $180^\circ$  field of view (FOV) charge coupled device (CCD), operating as a "pushbroom" imager capturing frames at regularly timed intervals on each orbit (Bell et al., 2009). For the visible (VIS) wavelength filters, the resultant raw data product was a long multi-filtered swath made up of individual frames captured along the orbit (Figure 4.1 panel b), with each frame containing five single filter "framelets." The VIS filters consist of a blue

( $437 \pm 32$  nm), green ( $546 \pm 40$  nm), orange ( $604 \pm 31$  nm), red ( $653 \pm 42$  nm), and near infrared (NIR,  $750 \pm 50$  nm) filter, each with an approximate down-track FOV of  $2^\circ$  and cross-track FOV of  $180^\circ$  (Bell et al. 2009).

The VIS filter data products from the PSP were downloaded manually from the PDS and run through a processing pipeline that was produced to calibrate the data according to the methods of Bell et al. (2009). Each multi-filter image was reduced in resolution through 8x8 pixel summing to reduce processing time, separated into the five VIS filters, and then run through the pipeline. The single filter images were cropped in width and length to exclude areas with high intensity limb scattering, and polar latitudes where ice is often condensed onto the surface. This cropping was necessary as the pixels with maximum reflectance values in each column of a cropped image were then assumed to contain Martian WICs, and isolated as the inputs for the remainder of the analysis. It was reasonable to assume that the brightest pixels across all VIS filters in images taken during the ACB were likely to be within cloudy regions once those areas were removed as Martian WICs have an average single scattering albedo (SSA) of 1.0 (Clancy et al., 2003) compared to Martian dust SSA of  $\sim 0.97$  (Wolff et al., 2009), and Martian WICs scatter relatively evenly in all visible wavelengths (Clancy et al., 2003).

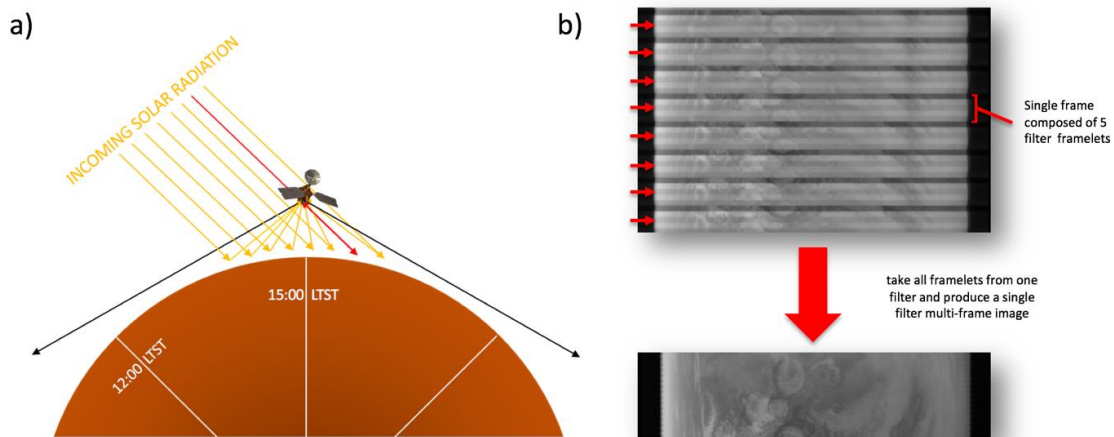
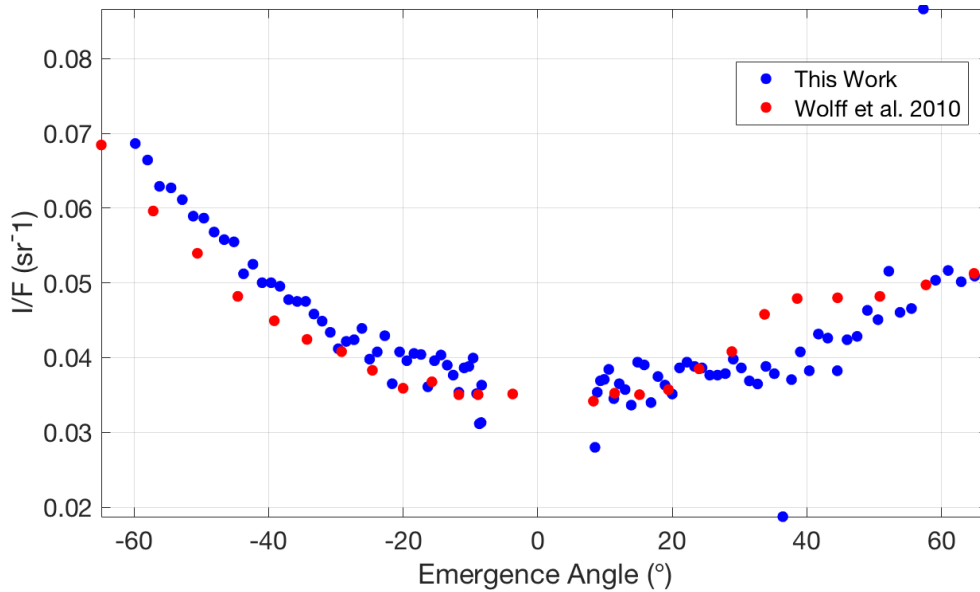


Figure 4.1: Panel a depicts a rough schematic of the typical viewing geometry of MARCI with MRO in its 3 am/3 pm sun-synchronous orbit, where it observes the equator at a local true solar time (LTST) of 15:00. With this geometry, MARCI is able to observe the  $180^\circ$  scattering angle in its filters' FOVs (as highlighted in this simple example by the red ray) and capture the  $180^\circ$  backscatter peak around the equatorial region (Cooper and Moores, 2019). Panel b displays the format of a raw multi-filter MARCI VIS image downloaded from the PDS, which then has to be separated into its five VIS filters to produce five single filter images, before it can be radiometrically calibrated.

To validate the success of the calibration, the cross-track reflectance (ratio of spectral radiance and flux) for band 1 (the blue filter) from our routine was compared to calibrated data for the image “P10\_004770\_2885\_MU\_00N178W” in Figure 1 of Wolff et al. (2010), and found to agree, as seen in Figure 4.2. The exact row of the image from which the blue filter data in Wolff et al. (2010) originated was not specified beyond mention of it being near the location of Spirit Rover, so a row was chosen close to the position of Spirit at the time of image capture. The discrepancy in rows of data being compared means our calibrated data is not able to be an exact match to that of Wolff et al. (2010), but it is in close agreement.



*Figure 4.2: The cross-track reflectances produced using our methods along a single row from the image “P10\_004770\_2885\_MU\_00N178W” were plotted alongside the reflectances from a near-by row in the same image from Wolff et al. (2010) to validate our calibration pipeline. The calibrated blue reflectances were multiplied by a factor of*

0.75 in Figure 1 of Wolff et al. (2010), and the same was done to our data for a better comparison.

## 4.2 Phase Function Determination

Following image calibration, the maximum reflectances from each column of each single-filter image were recorded along with their indexed pixel location and corresponding image label, to be used as an input for a SPICE kernel algorithm. SPICE is an information system produced by the Navigation and Ancillary Information Facility (NAIF), associated with NASA's Planetary Science Division (Acton, 1996). The information contained within the SPICE spacecraft, instrument, and ephemeris-based kernels was used in combination with multiple pre-written SPICE functions to develop a computational algorithm. This program determined and accounted for the distortion of the MARCI lens on the FOV of each of the CCD pixels, and provided an approximation of the regions of the Martian surface within the FOV of each pixel of interest, along with its respective illumination angles. As a result, the central Martian longitude and latitude in the FOV of each of the filters' max reflectance pixels were determined along with their corresponding solar incidence, emission, phase, and scattering angles. Once all the necessary parameters were determined as outlined above, the phase function was calculated using equation 5 from Wang et al. (2014):

$$P(\Theta, M) \approx \frac{4R_{c\lambda} \times (\mu + \mu_0)}{\omega_o} \left[ 1 - \exp\left(-\frac{\tau(\mu + \mu_0)}{\mu\mu_0}\right) \right]^{-1} \quad (4.1)$$

Equation 4.1 approximates the scattering phase function of a cirrus type cloud observed from orbit with single scattering (Wang et al., 2014), where  $P(\Theta, M)$  is the scattering phase function dependent on the scattering angle  $\Theta$ , and cloud microphysics,  $M$ . The cloud opacities ( $\tau$ ) came from integrated MCS water ice opacities (ranging from  $0.050 \pm 0.001$  to  $0.068 \pm 0.001$ ), binned for every  $10^\circ$  of  $L_s$ , averaged over the range of latitudes and longitudes contained within the PSP data that were converted from infrared to optical opacity by a conversion factor of 3.6 (Kleinböhl et al., 2011; Montabone et al., 2015 ;Guzewich et al., 2017). It should be noted that the MCS profiles have a mean profile lower limit of 13 km, and thus may not be capturing the complete cloud opacity. This is less of an issue with our focus on ACB clouds that typically extend from 10 km to 40 km in altitude (Clancy et al., 1996; Clancy et al., 2003). The ACB clouds were assumed to be capped at 40 km (Clancy et al., 1996; Clancy et al., 2003), and any ice opacity above was assumed to be upper atmosphere ice haze. The cosine of the emission and solar zenith angles were given by  $\mu$  and  $\mu_0$  respectively (Figure 4.3), for each relevant 8x8 summed pixel from the SPICE algorithm, along with a value for the single scattering albedo  $\omega_o$  of 1.0 (Clancy et al., 2003). The cloud reflectances  $R_{c\lambda}$  came from the radiometrically calibrated images, and account for the two-way transmissivity and the spectral reflectivity of the Martian surface via Equation 4.2:

(4.2)

$$R_{c\lambda} = \frac{R_{obs\lambda} - b_\lambda - c_\lambda}{\exp\left(-\frac{\tau_a}{\mu}\right) \exp\left(\frac{\tau_a}{\mu_0}\right)}$$

Equation 4.2 is rearranged from Equation 2 in Wang et al. (2014), solving for the corrected reflectance of a WIC ( $R_{c\lambda}$ ), using the calibrated reflectance ( $R_{obs\lambda}$ ) observed from orbit. The spectral reflectivity of the surface ( $b_\lambda$ ) was taken from Figure 1 of Adams and McCord (1969), while the spectral reflectivity of atmospheric gas ( $c_\lambda$ ) was taken to be negligible for the MARCI VIS filter band passes. Thus, the atmospheric gas above the clouds was assumed to be optically transparent, while the opacity of the dust and ice hazes above the clouds ( $\tau_a$ ) for the two way transmissivity correction were provided by the total summed ice and dust opacity from the seasonally averaged (within  $\pm 5^\circ L_s$ ) MCS profiles above 40 km, based on the previously outlined assumptions. As before, the MCS infrared water ice opacity was converted to a visible opacity by multiplying by a factor of 3.6, and the dust opacity was converted using a factor of 7.9 (Kleinböhl et al., 2011; Montabone et al., 2015; Guzewich et al., 2017).

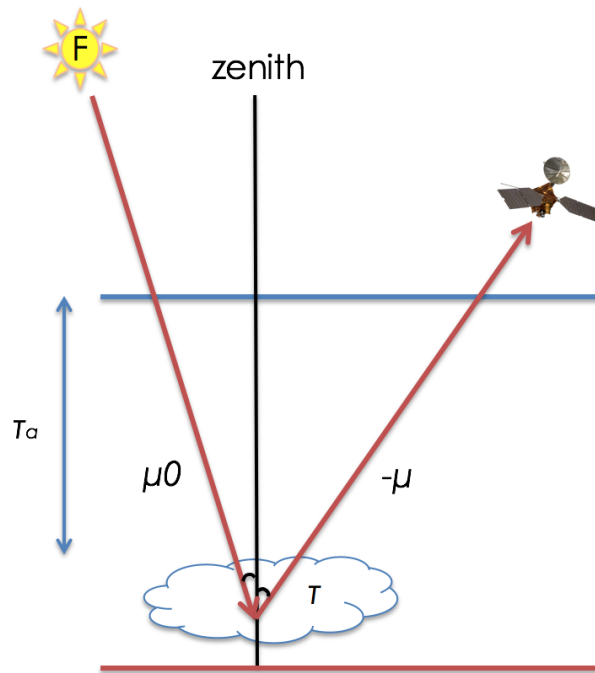


Figure 4.3: A two dimensional diagram depicting the physical relevance of the cosine of the emission and solar zenith angle ( $\mu$  and  $\mu_0$ ) variables in Equation 4.1, the WIC opacity ( $\tau$ ), and the opacity of the dust and ice hazes above the clouds ( $\tau_a$ ) in Equations 4.1 and 4.2. The sum of the emission and solar zenith angles is equal to the phase angle, and the scattering angle is equal to the phase angle subtracted from  $180^\circ$ .

Even though the MARCI data in this analysis was constrained to the ACB seasons of MY 28 and 29, we cannot discount dust activity occurring during this time which would also make a contribution to the radiance observed from orbit. Battalio and Wang (2019) catalogued dust events stemming from the Aonia-Solis-Valles Marineris (ASV) region for MYs 24-31, which is a southern hemisphere dust storm track infrequently activated during  $L_S=120^\circ$ - $180^\circ$  and is the source of the

most impactful, organized dust activity during the ACB season. Once all the phase function values were produced from the MARCI data using the methods described above, they were compared to the times and locations of the dust events outlined in Battalio and Wang (2019) for MYs 28 and 29, filtering out the data points that overlapped temporally and spatially. The remaining phase function data points were used to produce average phase function curves for each VIS filter, and for seasonal and geographic phase function analyses in the blue and red filters.

The standard phase function is typically normalized to unity over all scattering angles (Greenler, 1980), so the shape of the phase function curve along various scattering angles becomes the relevant factor for comparison with other models (as opposed to the unnormalized absolute magnitude). The unnormalized phase function magnitudes are also useful, as they provide context for other analyses with respect to relative cloud opacity and wavelength-dependent reflectance. It should be noted that the standard phase function normalization can be difficult or impossible to do when the experimentally derived phase function cannot be determined over the entire range of scattering angles from  $0^\circ$  to  $180^\circ$ , and so we adopted the methods of normalization from working with the MSL data that involve normalizing our derived mean phase function by the mean ACB phase function from Clancy et al. (2003) at the median scattering angle. The resultant normalized phase function curves were then used to constrain the seasonal dominant ice crystal geometries within the Martian WICs observed in this data set, and to probe the opposition surge.

# Chapter 5

## MARCI Dataset Results

### 5.1 Spectral Phase Function

Phase functions for each filter were calculated using Equations 4.1 and 4.2, and the data points located within the average radius of all the catalogued dust events from Battalio and Wang (2019) were filtered out. The resultant phase function point densities, averages, and upper-bounds for each VIS filter across all solar longitudes and geographic latitudes and longitudes were plotted and displayed in Figure 5.1. The point densities were produced by two-dimensionally binning the unnormalized phase function data from all seasons, latitudes, and longitudes for each filter into 124 bins across both the observed scattering angle range ( $50.3^\circ - 180.0^\circ$ ) and the unnormalized phase function magnitude. The number of points in each two dimensional bin was then divided by the total number of points in its respective scattering angle column. The averages and upper bounds of the phase function data in each scattering angle bin were determined and smoothed using a simple boxcar averaging function with a width of three data bins, plotted overtop of the densities.

## Point Densities and Averages of Filtered Phase Functions for All VIS Filters

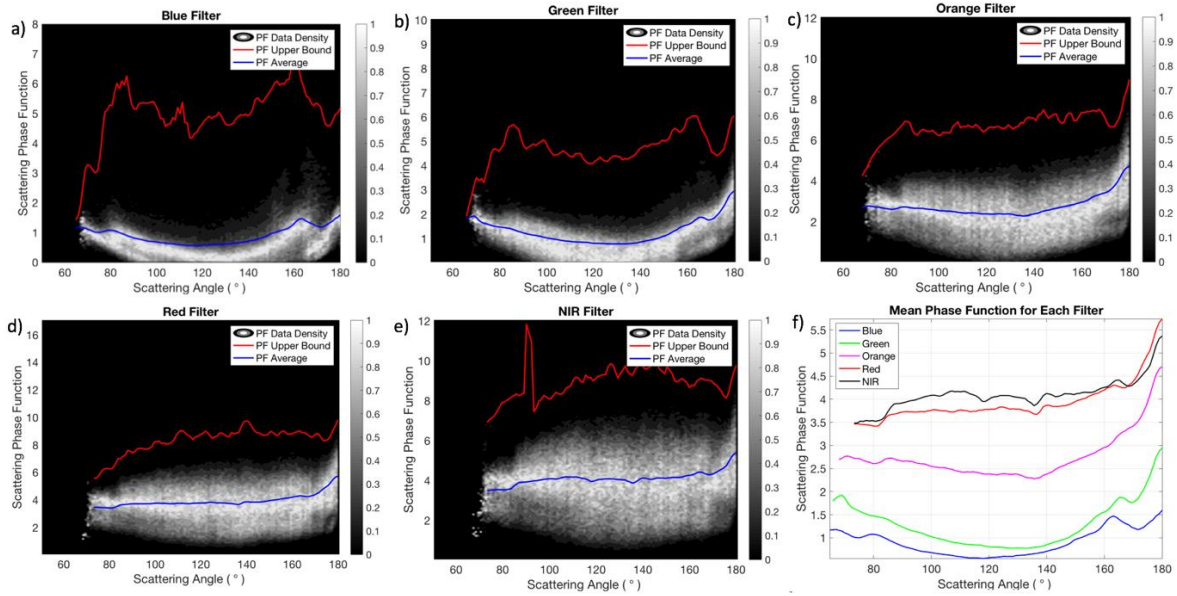


*Figure 5.1: The point densities of the filtered, unnormalized phase function data for each filter were produced by binning along both the scattering angle range and the phase function magnitude, and then dividing the number of data points in each two-dimensional bin by the total number of data points in its corresponding scattering angle column. The mean phase function curves and upper bounds of the point distributions along the scattering angle ranges were plotted overtop of the densities in blue, and red, respectively. The unnormalized mean curves for each filter were then plotted together in panel (f), to better compare their shapes and magnitude ranges. The phase function magnitude increases with wavelength along all scattering angles, and there is a noticeable evolution of shape with wavelength from convex to flat.*

From Figure 5.1, we observe an evolution of shape in both the cloud of point densities and the mean phase function curves, from convex in in the shorter

wavelengths to flatter in the longer wavelengths. The opposition surge is also visible in all the phase functions, in the form of a peak leading up to the 180° scattering angle. A possible explanation for the evolution of phase function shape from the blue to NIR filter will be addressed in Section 5.2.

Comparing the range of collective phase function magnitudes within all the VIS filters, and by extension the average phase function of the VIS filters (Figure 5.1), we can see the unnormalized magnitude increases with increasing wavelength, at all scattering angles. This agrees with the increase in spectral reflectivity of Mars' surface and dusty atmosphere with wavelengths in the range of MARCI's filter band passes (Adams and McCord, 1969 and Vincendon et al., 2014). This in turn affects in the magnitudes of the wavelength-dependent reflectances input into Equations 4.2 and 4.1. The phase function magnitude range for the blue filter is  $3.5 \times 10^{-5}$  to 7.5, with an average standard deviation of 0.69 for each scattering angle bin, while the range for NIR data is  $2.8 \times 10^{-2}$  to 18, with an average standard deviation of 1.3.

## 5.2 Geographic Analysis

The filtered unnormalized phase function data points in the blue and red filters were plotted in Figure 5.2 with respect to their latitude and longitude (determined using SPICE for the centre of each 8x8 summed pixel) in order to observe their geographic distribution and magnitude. As outlined in Chapter 4, the data points that were analyzed in our SPICE algorithm came from the radiometrically calibrated, summed, and cropped image pixels with maximum reflectance values in each column of each filter for each image, thus the location of

the data points vary for each filter. From Figure 5.2, we see that the majority of the red and blue filter data points are acquired between  $-20^{\circ}$  and  $+70^{\circ}$  latitude, with two zonal bands around  $\sim+20^{\circ}$  and  $\sim+40^{\circ}$  in blue, and one zonal band around  $+30^{\circ}$  in red. Fewer data points are acquired in the southern hemisphere compared the northern hemisphere, as MRO's orbit produces a seasonal offset in latitude coverage. This in combination with uniform image cropping to exclude the polar caps at all times of year led to data focused towards the northern hemisphere at the times of interest for this study. This offset is not of concern as it includes the primary latitudinal range of the ACB from  $-10^{\circ}$  to  $+30^{\circ}$  (Wolff et al., 1999; Clancy et al., 1996).

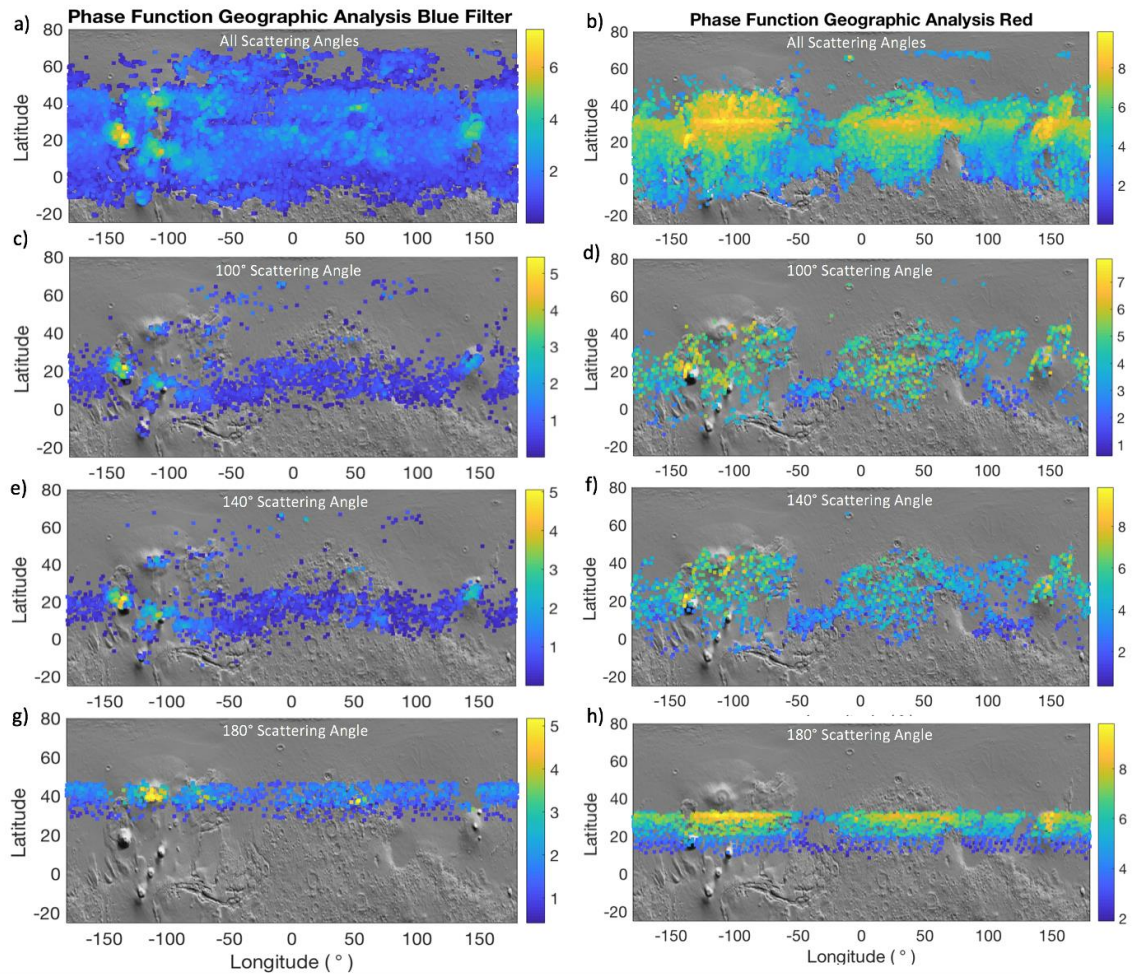


*Figure 5.2: The filtered and unnormalized phase function data points for the blue and red filters are plotted with respect to their latitude and longitude to analyze their geographic distribution. Panels (a) and (b) contain phase function values at all scattering angles, while panels (c-h) contain phase function values at the fixed scattering angle listed. The color axis provides the unnormalized phase function magnitude, which provides some context regarding reflectance in panels (c-h). In both filters, where the peaks in magnitude (yellow points near Latitude 20°N and Longitude 140°W) likely correspond to orographic clouds over Olympus Mons. Other peaks likely*

*correspond to orographic clouds around Alba Mons, Tharsis Montes, and Elysium Mons.*

From Figure 5.2, the blue filter data points are more evenly spread across Martian longitudes between  $-10^{\circ}$  and  $+50^{\circ}$  latitude than the red data, and there are some noticeable gaps in the red data between  $-45^{\circ}$  and  $-20^{\circ}$  longitude within  $+15^{\circ}$  and  $+30^{\circ}$  latitude, and between  $+50^{\circ}$  and  $+80^{\circ}$  longitude below  $+20^{\circ}$  latitude. Blue filter data points are present in these regions but they are lower in magnitude, indicating that they likely correspond to optically thin clouds with low reflectances. In this scenario, the optically thin clouds produce the maximum reflectance values in their column for the blue filter (and thus are selected for processing through our algorithm), but in the red filter, a dust or surface-related feature at a different latitude had a consistently higher spectral reflectance, and was selected instead. This interpretation is strengthened by the comparison of the location of the red data points to the regions of high surface albedo measured by Mars Express in Vincendon et al. (2014), and the dust cover index map of Ruff and Christensen (2002). It provides additional context for the evolution of the shapes of the mean phase function curves in Figure 5.1 from convex in the blue, to a flatter shape in the longer wavelengths. This is indicative of contamination from the Martian surface and dust in the longer wavelength filters, which we would expect, as Martian dust and surface reflectivities are much greater in the green to NIR wavelengths than blue (Adams and McCord, 1969 and Vincendon et al., 2014). Thus, the blue filter phase function is the best choice for constraining the observed phase function of Martian WICs with

this dataset (as it will have the lowest surface and dust contamination), especially for the purpose of comparing it to models and other derived curves.

Looking at the distribution of phase function magnitudes in all panels of Figure 5.2, there are peak magnitudes observed in both filters around the locations of Olympus Mons, Tharsis Montes, Alba Mons, and Elysium Mons, indicating repeated detections of optically thick orographic clouds at these high elevation locations. The Mars Analysis Correction Data Assimilation (MACDA) (Montabone et al., 2014) shows the time-mean wind velocities at 2 pm at 15-40 km altitude between  $L_S=141^\circ-157^\circ$  in MY 24 to be in south-western direction to the south-west of Olympus Mons, Alba Mons and Elysium Mons (not shown). This suggests a leeward flow down the slopes of these mountains in these particular areas, and the lack of blue data points observed most easily in panel a could be explained by adiabatic warming of the descending atmospheric parcels and sublimation of clouds.

The zonal band centred on  $+20^\circ$  latitude in Figure 5.2 (a) is located within the typical latitudes expected for the ACB (Wolff et al., 1999; Clancy et al., 1996), however the  $+40^\circ$  latitude band extends further north, and corresponds to the single band in panel g caused by the opposition surge, likely from optically thin water ice hazes (Cooper and Moores, 2019). In the red filter however, the band corresponding to the opposition surge occurs at a lower latitude (closer to  $+30^\circ$ ) as a result of the filter placement on the CCD, which has the red filtered portion of the CCD observe the  $180^\circ$  scattering angle at a different latitude than the blue filter (Cooper and Moores, 2015).

## Blue Phase Function Geographic Analysis

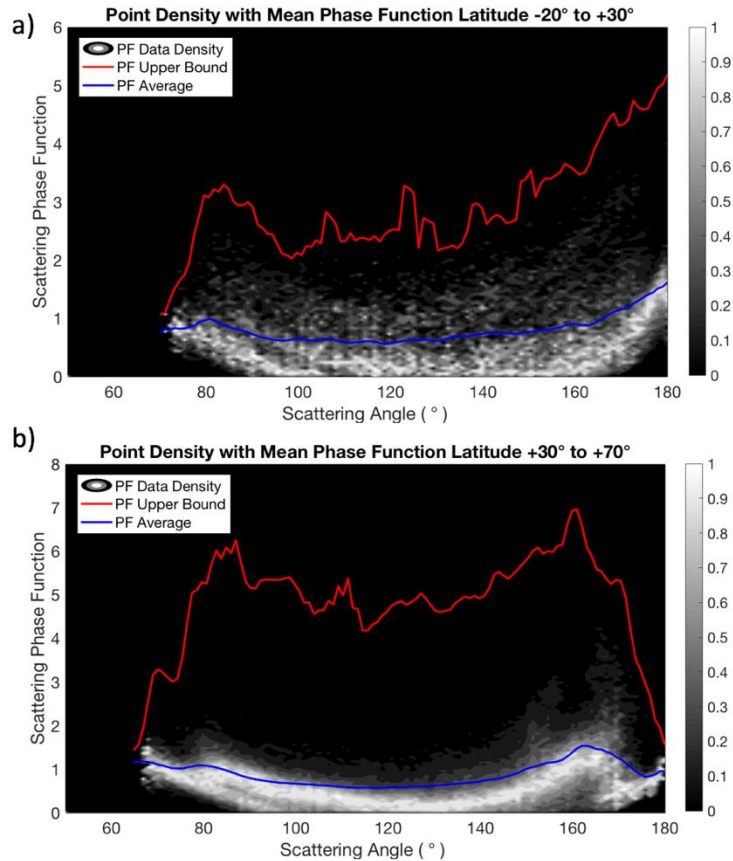


*Figure 5.3: The filtered unnormalized phase function point densities for the blue and red filters were separated into two latitude ranges across all seasons, with latitudes from  $-20^{\circ}$  to  $+30^{\circ}$  being the typical ACB range, and latitudes greater than  $+30^{\circ}$  being within the typical range of northern polar hood clouds and water ice hazes. The blue filter data varies between latitude ranges in both shape and distribution of points. The  $180^{\circ}$  opposition surge is greater in data corresponding to latitudes greater than  $+30^{\circ}$ .*

The blue unnormalized phase function data was divided into two latitude regions in Figure 5.3: data points at latitudes less than or equal to  $+30^{\circ}$ , and data

points at latitudes greater than  $+30^\circ$ . Given that a majority of the data is focused between  $-20^\circ$  and  $+70^\circ$ , these ranges were chosen to separate the typical ACB latitudes ( $-10^\circ$  to  $+30^\circ$ ) from those where we might expect northern polar hood (NPH) clouds ( $>+30^\circ$ ) and ice hazes.

The geographic blue filter phase functions vary in shape and distribution of magnitude along all scattering angles between the two latitude ranges. Referring back to panel g of Figure 5.2, it is clear that the  $180^\circ$  scattering angle is only observed by the blue portion of MARCI's CCD over a distinct latitude range, which extends from  $+27^\circ$  to  $+46^\circ$  over all seasons. From Cooper and Moores (2019), we saw that the observed scattering angles vary with latitude and filter, and if you extrapolate beyond that single example, it also changes with seasonal illumination for a constant latitude. As the range of latitudes in which the  $180^\circ$  scattering angle is observed extends into both the latitude ranges in Figure 5.3, we see the  $180^\circ$  peak in both. From panel g of Figure 5.2, we can see the phase function values at that scattering angle are higher for the higher end of the range of latitudes. This agrees with the unnormalized phase function values in the  $180^\circ$  scattering angle bins of Figure 5.3, with a mean value of 0.96 for data at latitudes less than  $+30^\circ$  and 1.6 for data at latitudes greater than  $+30^\circ$ .

To summarize, the unnormalized phase function data points in the blue and red filters were plotted with respect to their longitude and latitudes for different scattering angles, and the blue phase function magnitude point densities were plotted with respect to two latitude ranges. They were divided by a latitude of  $+30^\circ$  to isolate potential differences in clouds forming within and outside of the classic

ACB latitudes, and to observe the effect of topography on the data points selected. Topographic features such as Olympus Mons, Alba Mons, Elysium Mons and Tharsis Montes all produced high opacity orographic clouds visible in the blue and red data, and it became clear that beyond those features, the red data had a great deal of surface and dust influence. This confirmed that the blue filter data was the best choice for analyzing the phase function of Martian WICs, with the least contamination from Martian surface and dust.

### 5.3 Seasonal Analysis

The blue filter phase function in Figure 5.1 (a) had data from all solar longitudes in the ACB seasons probed for this study, so in order to isolate the fluctuations caused by seasonal variations of cloud opacity, the investigation period was broken down into smaller solar longitude “seasons” for each MY. The blue filter was divided into solar longitude ranges of  $L_S = 42^\circ\text{-}84^\circ$ ,  $L_S = 85^\circ\text{-}127^\circ$ , and  $L_S = 128^\circ\text{-}170^\circ$  (because MRO reached Mars at  $\sim L_S = 128$  in MY28, only the last  $L_S$  range could be investigated for that year). Phase function point densities were produced for each of the miniature seasons, along with an average curve and distribution upper-bound. The mean curves from each season were plotted overtop of their point densities in panels a-d of Figure 5.4, and all together in panel e for a more direct comparison of their unnormalized magnitudes and shapes.

## Blue Phase Function Seasonal Analysis

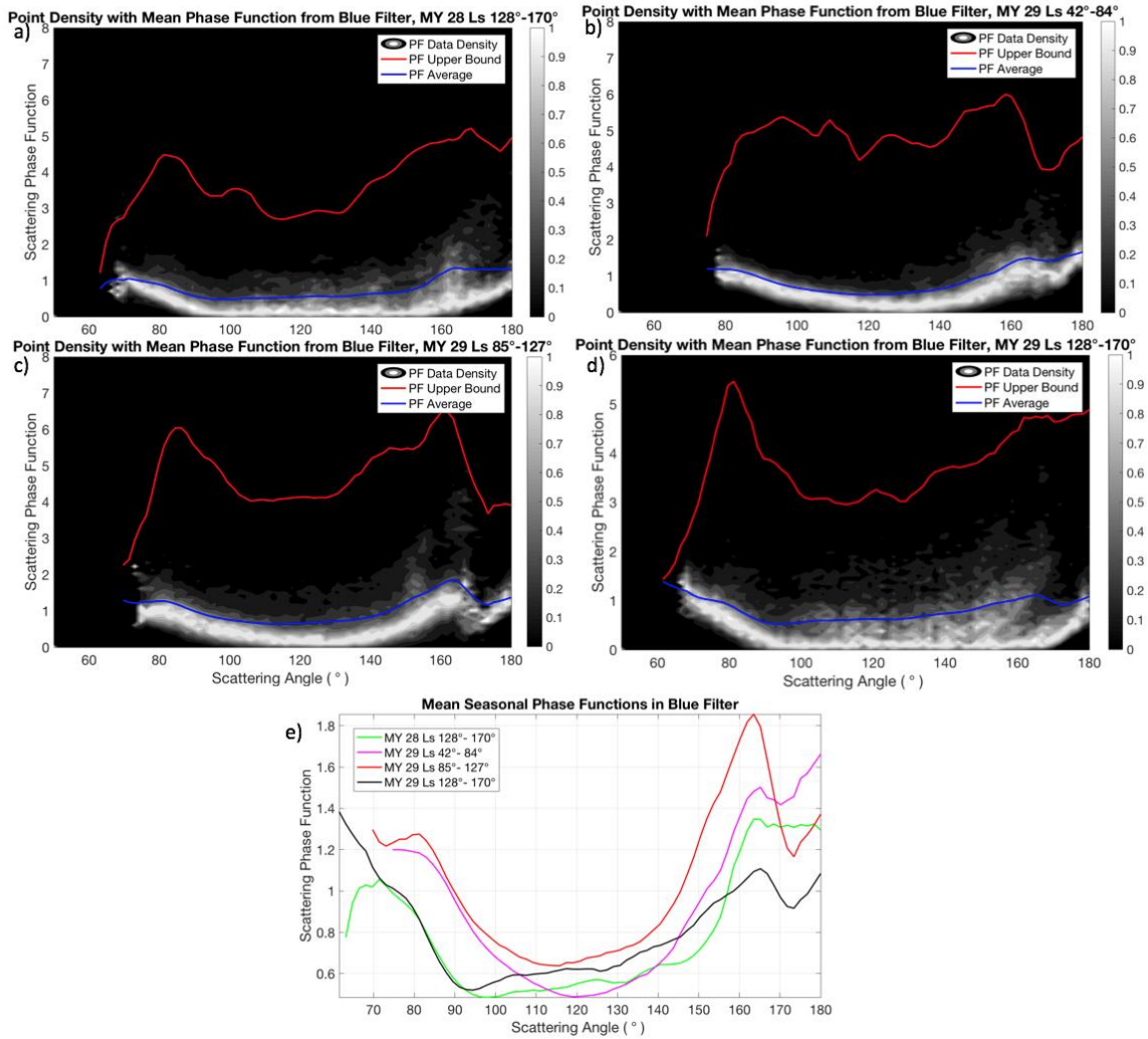


Figure 5.4: The filtered unnormalized seasonal phase function point densities were produced for the blue filter over solar longitude ranges of  $L_s = 42^\circ\text{-}84^\circ$ ,  $L_s = 85^\circ\text{-}127^\circ$ , and  $L_s = 128^\circ\text{-}170^\circ$  for MYs 28 and 29 (because MRO reached Mars at  $\sim L_s = 128$  in MY28, only the last  $L_s$  range could be looked at for that year). The mean curves of the distributions were plotted atop the density plots and together in the first panel. The  $L_s = 85^\circ\text{-}127^\circ$  range for MY 29 has the highest magnitude across all scattering angles due most likely to a peak in ACB cloud opacities. The  $L_s = 128^\circ\text{-}170^\circ$  range for both MYs

*had more variability than the other miniature “seasons”, with lower magnitudes, and similar shapes.*

The MY 29  $L_S=85^\circ-127^\circ$ , season had the most consistently high magnitudes with an average phase function magnitude of 1.0, followed by the MY 29  $L_S = 42^\circ-84^\circ$  season (0.92) and  $L_S=128^\circ-170^\circ$  from both MYs (0.80, and 0.82, respectively). Additionally, we can also note the variation in the distribution of the phase function data for each scattering angle bin between the miniature seasons.

We can provide some additional context to the blue seasonal phase functions shown in Figure 5.4, as well as the geographic distribution of the un-dust-filtered phase function data in the blue and red filters from Figure 5.2, by looking at Figure 5.5. The unfiltered and unnormalized phase function data points from all scattering angles, as well as a slice through the  $165^\circ$  and  $180^\circ$  scattering angles, are plotted with respect to latitude and  $L_S$  for the blue and red filter data. The colour axis is the unnormalized phase function, and the overlaid points correspond to the centres of the catalogued ASV dust events, with red indicating a dust-cloud mix, and black indicating no observed clouds.

## Phase Function Latitude and Temporal Distribution and Dust Event Comparison

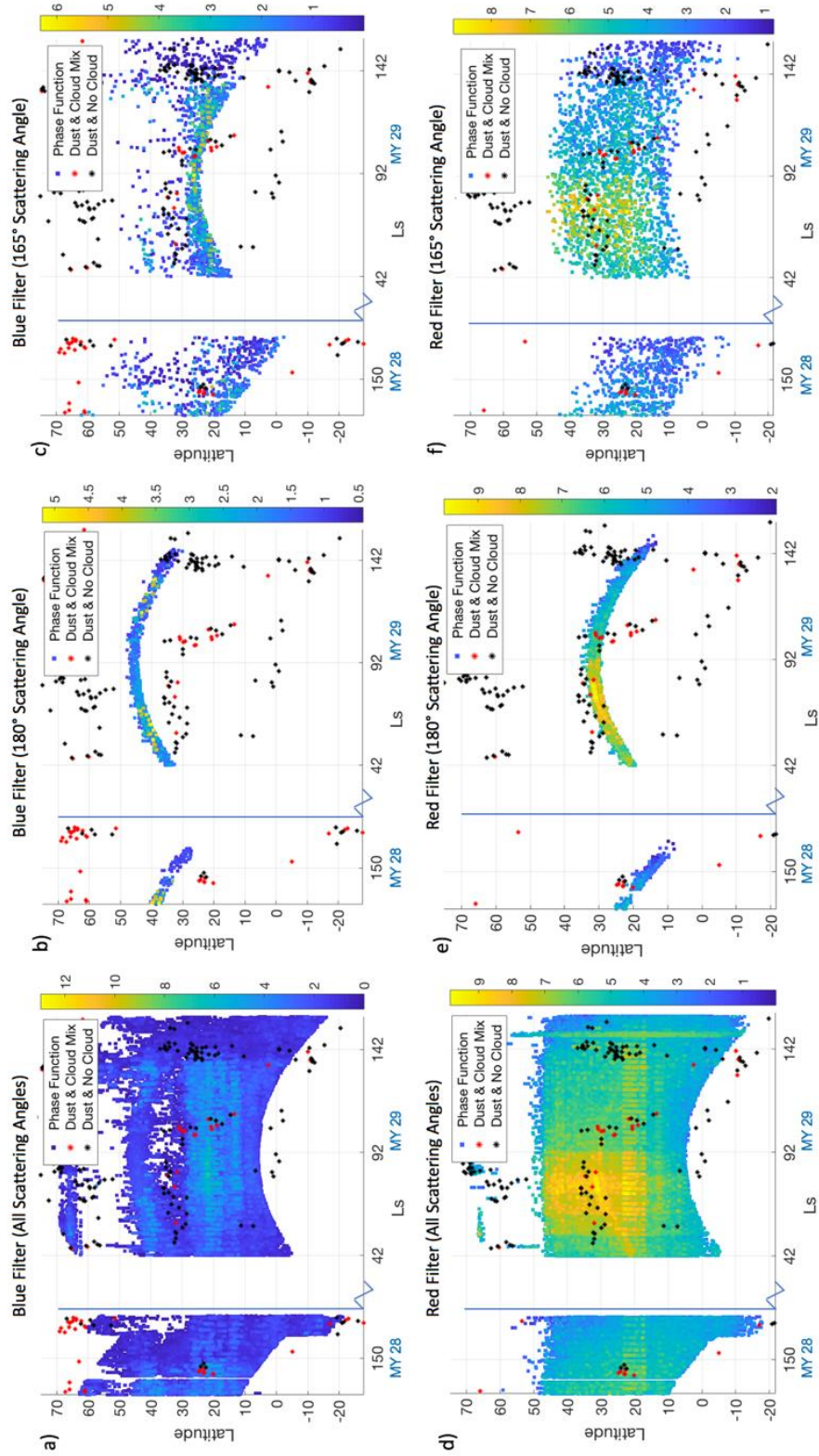


*Figure 5.5: The resultant unnormalized and unfiltered phase function values for the red and blue filters are plotted with respect to Martian latitude and solar longitude over the periods of interest in MYs 28 and 29. The colour axes correspond to the phase function values for each filter, and the overlaid black and red points correspond to the centres of dust events (without observed clouds, and with an observed dust-cloud mix, respectively) catalogued by Battalio and Wang (2019).*

In MY 29, within  $+28^\circ$  and  $+35^\circ$  latitude there are 22 localized dust storms that persist between  $\sim L_S=55^\circ-95^\circ$  and are present in both filters. In the case of the blue filter data in panel a, these particular dust storm centroids overlap with lower phase function magnitudes and a reduction of data points for this latitude range that is not present in the red. This region is on the margin of the typical ACB latitude range, and that in combination with dust lifting from the regional storms could have inhibited cloud formation in this area until  $\sim L_S=130^\circ$ . In the red filter however, these dust storm centroids overlap with the highest phase function magnitudes observed in the red data in panel d, which is partially a result of the fact that they overlap with the latitude range associated with the opposition surge, but is also due to the high reflectivity of Martian dust in red wavelengths. Dust appearing in the unfiltered red phase function data is yet another confirmation that the blue filter data is the least dust and surface contaminated candidate for our analyses that take place in Chapter 6.

Higher magnitude phase function bands centered between  $+5^\circ$  and  $+25^\circ$  exist in both filters during both MYs, and correspond to the typical latitude range

expected for ACB clouds. In panel c, data points at a single scattering angle of  $165^\circ$  are shown, and we can see that generally, a majority of the data points correspond to ACB clouds along all solar longitudes. This is the likely cause of the peak around the  $165^\circ$  scattering angle in the blue filter phase functions, and would explain why the peak is not present in the phase function for data at latitudes greater than  $+30^\circ$  in Figure 5.3, where the  $165^\circ$  scattering angle corresponds to lower opacity WICs beyond the typical ACB range (Figure 5.5 (c)). It also aligns with the variation in magnitude of the  $\sim 165^\circ$  peak in the seasonal phase functions of Figure 5.4 (e): the higher unnormalized magnitudes of the phase function around the  $165^\circ$  scattering angle from  $L_S=42^\circ$ - $127^\circ$  in MY 29 correspond to the increase in phase function magnitude at the  $165^\circ$  scattering angle with respect to season in panel c of Figure 5.5.

The peak in red phase function magnitude around  $\sim L_S=146^\circ$  corresponds to the plethora of cloudless dust storms within the largest ASV sequence identified in Battalio and Wang, (2019), that triggered a rare sequence of dust activity in Chryse in MY 29. A peak in the blue phase function magnitude was not observed for this time, and furthermore, the dust event centroids at this  $L_S$  coincide with a uniform drop-off in blue phase function over all latitudes and scattering angles in Figure 5.5 (a-c), for the remainder of the investigation period. This large-scale dust event likely triggered a quick decay of the ACB season for MY 29, and inhibited the development of NPH clouds due to increased atmospheric temperatures (James et al., 1987).

# Chapter 6

## MARCI Data Discussion

### 6.1 A Closer Look at the Opposition Surge

The opposition surge occurs at the  $180^\circ$  scattering angle frequently captured in MARCI images, and is amplified by the presence of Martian WICs to the point that it can produce an artifact with a rainbow-like appearance when VIS single filter images are combined to produce a false-colour composite RGB image (Cooper and Moores, 2019). Thus, the  $180^\circ$  peak should be represented in the phase function of Martian WICs (and we see it in all of our derived curves) as it is the only scattering phenomenon we have been able to observe from water ice crystals suspended in the Martian atmosphere.

The Mars Phoenix lander was equipped with a lidar, and Dickinson et al. (2011) used the lidar derived water ice extinctions to estimate the ice water content (IWC) using the empirical relationship from in situ measurements of terrestrial cirrus clouds, that IWC (in units of  $mg/m^3$ ) is equal to the WIC extinction (in units of  $km^{-1}$ ) multiplied by a factor of 10. In order to test this empirical relationship with our observed backscatter, we used the mean phase function values in the  $180^\circ$  scattering bin for the blue filter to minimize dust and surface influence, normalized in the method of the MSL data. The mean normalized phase function value in the  $180^\circ$  scattering angle bin for the blue filter ( $0.422 \pm 0.3 \times 10^{-2} \text{ sr}^{-1}$ ) represents the

observed backscatter from Martian WICs, and thus can be used in combination with the lidar ratio, the lidar equation, and equation 1 from Moores et al. (2011), to test the relationship between IWC and integrated extinction (optical depth), in the atmospheric column. Equation 6.1 is the resultant relationship between backscatter ( $\beta$ ) and IWC, where  $\alpha$  is the effective ice particle radius (a mean value of 2.75 microns for ACB clouds; Clancy et al., 2003), and  $\rho$  is the density of water ice:

(6.1)

$$\beta \cong \frac{1}{4\pi} \left( \frac{3 IWC}{2 \alpha \rho} \right)$$

The lidar ratio ( $S$ ) can be given by Equation 3 from Shin et al. (2018):

(6.2)

$$S = \frac{4\pi}{\omega_o F_{11}(180^\circ)}$$

Where  $F_{11}(180^\circ)$  is the element in the Müller scattering matrix at a scattering angle of  $180^\circ$ . Given the value of the single scattering albedo of water ice clouds already taken to be 1, and the mean value of our normalized derived  $180^\circ$  phase function to be  $0.422 \pm 3 \times 10^{-3} \text{ sr}^{-1}$ , the resultant mean lidar ratio is equal to 29.8 *sr*. This lidar ratio is about a factor of 2 greater than the lidar ratio for the clouds observed by Phoenix (Whiteway et al., 2009), and is also equal to the ratio of extinction and backscatter, and thus the relationship between extinction ( $\sigma$ ) and IWC can be shown via Equation 6.3:

(6.3)

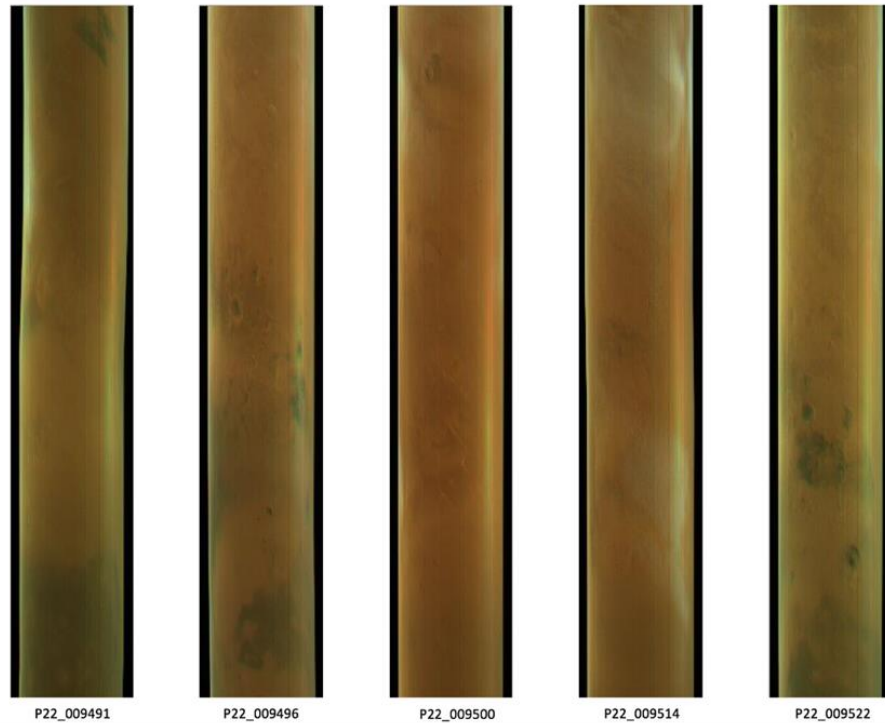
$$\sigma \cong \frac{S}{4\pi} \left( \frac{3 IWC}{2 \alpha \rho} \right)$$

Rearranging Equation 6.3 for IWC, we find that IWC is equal to the extinction multiplied by a mean factor of 5 for the mean 20 micron ice particles modeled to have been observed by Phoenix (Moores et al., 2011). The factor of 2 between our results and the relationship observed by Dickinson et al. (2011) was likely caused by the difference in the mean range of ice crystal sizes between the NPH and ACB, which is seen in the difference between our derived lidar ratios (also a factor of two). For the case of ACB ice crystals with a mean radius of 2.75 microns, the IWC was found to equal the extinction multiplied by a factor of 0.7. Given the range of magnitudes between these two factors, we can say that it is difficult to accurately derive the IWC from extinction for all ice crystals, as it requires knowledge of the mean radius of the ice crystals within the WICs observed, so a general empirical relationship for all sizes is not applicable.

The opposition surge was further probed by a sensitivity study of the half-width-half-max (HWHM) of the observed feature in the blue and green filters to minimize contributions from the surface, as in Cooper and Moores (2019). Five images (P22\_009491\_1083\_MA\_00N201W, P22\_009496\_1084\_MA\_00N337W, P22\_009500\_1086\_MA\_00N087W, P22\_009514\_1091\_MA\_00N109W, and P22\_009522\_1094\_MA\_00N327W) were randomly chosen from the middle of the ACB season, and calibrated using the methods outlined in Chapter 4. The red, green, and blue filters were combined to make a composite RGB image for each, as shown in Figure 6.1. When an RGB image is produced, the opposition surge (which appears

on the right of each of the images in Figure 6.1) is smeared along multiple latitudes and appears to change colour. Cooper and Moores (2019) demonstrated that this is an illusion caused by VIS filters permanently mounted on different regions of the CCD, in combination with the MARCI lens distortion. As a result, different filters observe different scattering angles at different latitudes in the same image (Figure 1(c) in Cooper and Moores, 2019).

a) Opposition Surge in MARCI RGB Composites MY 29 Ls=108°-109°



b)

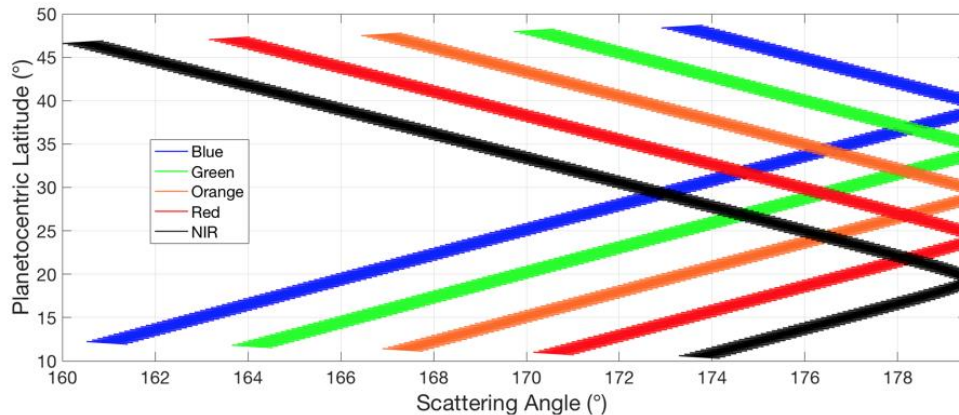


*Figure 6.1: Panel a contains cropped MARCI images from the ACB season are shown, with the commonly observed “rainbow” artifact that is produced by the opposition surge in different filters at different latitudes (Cooper and Moores, 2019). The red, green and blue filter swaths are overlaid to produce an RGB MARCI frame, and the opposition surge is visible as the bright multi-coloured region on the right side of each swath. This effect is caused by each filter observing the 180° scattering angle, and thus the opposition surge at a different latitude due to their varying FOV, as seen in panel b.*

Reflectances and SPICE-derived latitudes along the opposition surge were used to probe the HWHM by fitting the peak in reflectance for each filter to a gaussian curve; this was done for all five images in the blue and green filters to minimize contributions from the surface. The resultant HWHMs for images listed in Figure 6.1 were found to be (in order): 3.94°, 1.95°, 3.14°, 1.66°, 1.93° in the blue filter, and 3.84°, 2.23°, 3.80°, 2.32°, and 1.74° in the green filter. This led to an average HWHM of 2.52° for blue, and 2.79° for green, compared to the values of 3.42° and 3.43° respectively from the single example in Cooper and Moores (2019). A great deal of cloud activity was visible in the Mars Global Daily Maps for all these images (MGDMs; Wang et al., 2018), which suggests a strong presence of ice aerosols are producing this overtly strong backscatter effect. This explanation is further justified by the fact that the HWHM of the opposition surge is within the range of values expected for WICs (approximately 2°- 5°; Chepfer et al., 2002; Yang and Liou, 1996; Yang et al., 2010), compared to values for the Martian dust or the

surface (on the order of  $10^\circ$  or greater; Clancy et al., 2003 and Soderblom et al., 2006).

## 6.2 Phase Function Normalization and Habit Analysis

The mean seasonal blue filter phase function curves were normalized using the same technique as the MSL data, which is to normalize the data by the average value of the TES-derived aphelion type 1 and type 2 WIC phase functions (Clancy et al., 2003) at the median observed scattering angle. The five mean seasonal phase functions from Figure 5.4 (normalized in Figure 6.2) were then compared to the seven modeled ice crystal phase functions from Yang and Liou (1996) and Yang et al. (2010), the observationally derived phase function from the PFSS, and the six RT-fit phase functions from Clancy and Lee, (1991) and Clancy et al., (2003).

### Ice Crystal Habit Analysis

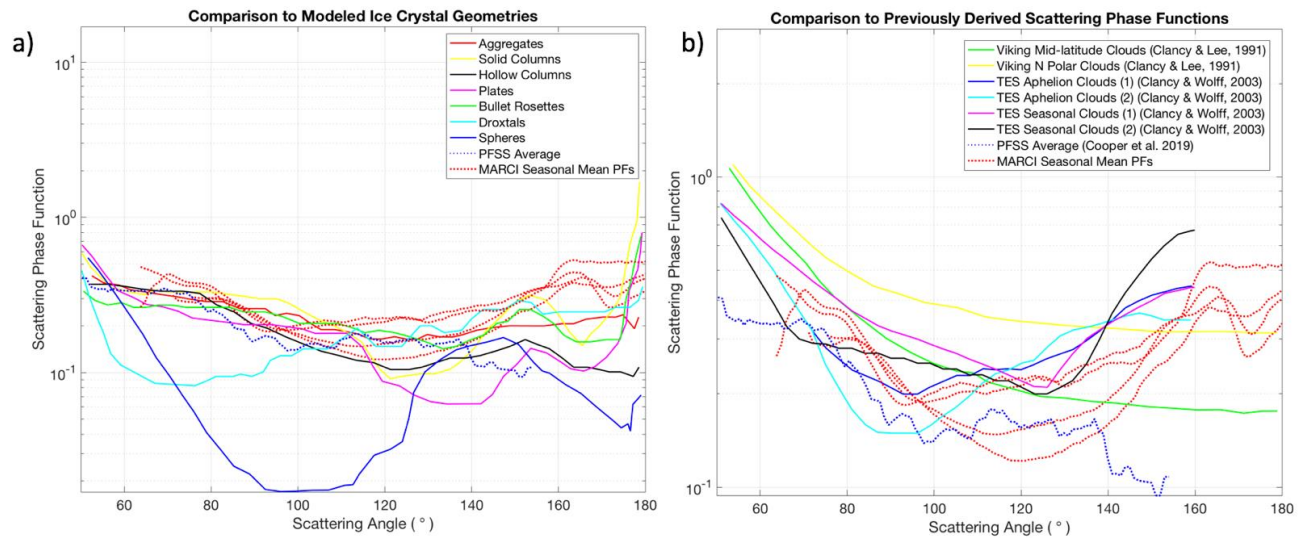


*Figure 6.2: The five seasonal mean phase functions from Figure 5.4 were normalized and are shown superimposed over the seven modeled ice crystal geometries from Yang and Liou (1996) and Yang et al. (2010) in panel a. In panel b, those same five phase functions are displayed with our observationally derived phase function from MSL, and the six RT-fit phase functions from Clancy and Lee, (1991) and Clancy et al., (2003) to provide context (note the axis range differences between panels a and b).*

Figure 6.3 shows the results of the weighted chi-squared goodness of fit tests for the models from Yang and Liou (1996) and Yang et al. (2010), with their subsequent p-values. For all seasons, the ice crystal geometries most probably observed within the MARCI data were aggregates (with p-values ranging from 0.771 - 0.869) closely followed by bullet rosettes (0.727 to 0.833) and solid columns (0.745 to 0.852), while the least likely were spheres (0.219 - 0.277). Droxtals had greater probabilities for this data set than Cooper et al. (2019), with p-values ranging from 0.621 to 0.771, compared to 0.35 previously.

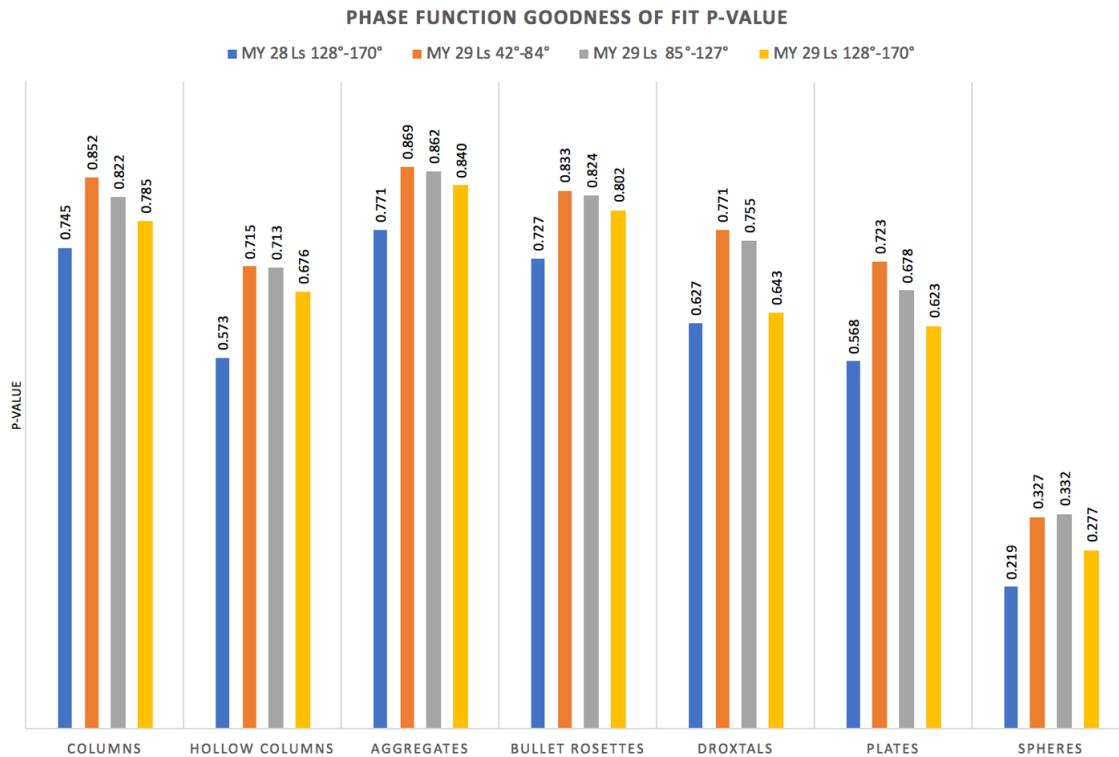


*Figure 6.3: The normalized mean seasonal phase functions were compared to seven modeled ice crystal phase functions from Yang and Liou (1996) and Yang et al. (2010). A weighted chi-squared analysis and p-tests were used to determine goodness of fit. The results show to first order that spheres are the least probable geometries within all seasons, while aggregates are most probable, closely followed by bullet rosettes and solid columns.*

From Whiteway et al. (2004), and Yang et al. (2003) we know that in a typical Terrestrial WIC, ice crystal formation occurs at the top of the cloud, then the ice crystals grow, fall, and sublimate as virga (observed on Mars by Whiteway et al., 2009). Whiteway et al. (2004) sampled Terrestrial cirrus clouds over Australia and found a mix of rosettes at the highest levels along with columns and irregular

shapes, while larger aggregates and irregular shaped crystals were present at the bottom of the clouds. Yang et al. (2003) discusses sampled mid-latitude cirrus and found small droxtals at the highest levels with temperatures below 223 K, pristine plates and columns in the mid-levels, and larger rosettes and aggregates at the lowest levels.

Both of these publications agree that aggregates are typically found in the lower portion of a WIC, that aggregates are typically larger than the more “pristine” crystals like plates and columns, and that the smallest components exist at the top of the cloud. This aligns with the fact that we were observing Martian WICs from the surface with MSL and found aggregates to best fit their derived phase function, as larger aggregates would provide the greatest contribution of detected scattering from below the WICs. Aggregates had the best fit for all seasons in this analysis as well, and even though we are observing from above, the fact that these ice crystals are likely the largest in size means that they should still contribute a large amount to the detected scattering. The remaining modeled geometries (with the exception of spheres) from Yang and Liou (1996) and Yang et al. (2010) had better fits for this work than they did for the PFSS, which could be due to the fact that observing the WICs from above allows for easier detection of scattering contributions from smaller crystals at higher elevations.

Droxtals had the most notable jump in p-value with an average value for all the seasons of 0.699, compared to the PFSS results with a p-value of 0.35. This is not surprising, given that Yang et al. (2003) suggests that these are the smallest ice crystals forming at the top of a cirrus cloud. If droxtals were present at the top of the

Martian WICs observed by MSL and they had an average radius that was approximately half that of the aggregates at the bottom of those same WICs, they would have been hard to detect using surface-based methods.

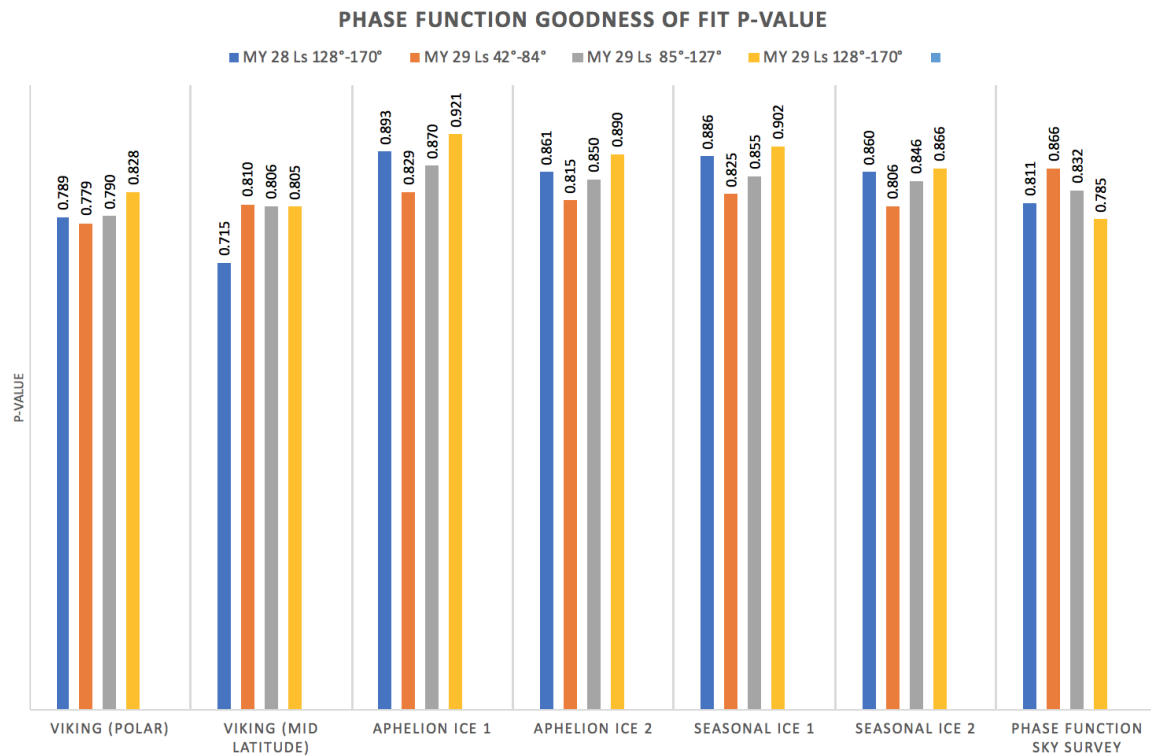


*Figure 6.4: The normalized seasonal phase functions were compared to the mid-latitude and polar phase functions from Viking EPFs (Clancy and Lee, 1991), aphelion and seasonal ice aerosol phase functions from Clancy et al. (2003), and the aphelion phase function sky survey results via chi-squared analyses and a p-test. The Aphelion Ice 1 from Clancy et al. (2003) had the highest p-values for all seasons except the earliest season in MY 29, which fit the derived curve from the PFSS.*

The normalized mean seasonal phase functions were also compared to the mid-latitude and polar phase functions from Viking EPFs (Clancy and Lee, 1991), the aphelion and seasonal ice aerosol phase functions from Clancy et al. (2003), and the aphelion phase function sky survey (PFSS) results. The results of the weighted chi-squared and p-test analysis are shown in Figure 6.4, with the greatest agreement to aphelion ice 1 from Clancy et al. (2003) (p-values ranging from 0.829 to 0.921) for all seasons except MY 29  $L_S=42^\circ-84^\circ$ , which best fit our PFSS phase function with a p-value of 0.866. The p-values for the phase functions from Clancy and Lee (1991) and Clancy et al. (2003) were higher for this data set than the data from the MSL data, with ranges from 0.806 to 0.921, compared to a range of 0.48 to 0.62 previously. The surface-derived phase function from Cooper et al. (2019) had the poorest fit for the MY 29  $L_S=128^\circ-170^\circ$  season (p-value of 0.785), but fit the remaining two seasons moderately well.

In Clancy et al. (2003), the aphelion (type 2) ice aerosol is postulated to be a “spheroidal” geometry, and it had a better fit than the seasonal ice (type 1), which is postulated to have a more “crystalline” shape. The droxtal habit would likely better represent the aphelion/type 2 ice from Clancy et al. (2003), as Yang et al. (2003) states that it is a more realistic crystal geometry for small ice crystals hypothesized to be “quasi-spherical”, while still maintaining an aspect ratio of unity. Clancy et al. (2003) also puts forward the possibility of the type 1 aerosol taking the form of ice Ic, a variant from the typical form of ice Ih on Earth which produces the hexagonal-based shapes modelled by Yang and Liou (1996) and Yang et al. (2010). Ice Ic is a form of water ice where the oxygen atoms are arranged in a cubic or diamond

structure and can lead to isometric forms like octahedrons or dodecahedrons. Gooding et al. (1986) investigated the role of dust particles in the atmosphere for deposition of water vapour to form WICs. They found that vapour/solid transitions in the Martian atmosphere favour ice Ic formation, and that the overall best substrate for the nucleation of other condensates is ice Ic, therefore, the most effective mineral substrates for condensate formation on Mars might be those that are most effective at nucleating ice Ic. From Figure 14 we can see that the potential ice Ic (seasonal) aerosols from Clancy et al. (2003) were the second best fitting habit behind the aphelion aerosols, and suggest we could be observing both water ice variations, with one potentially nucleating the other.

The Viking polar WIC phase function from Clancy and Lee (1991) was the poorest fitting phase function for the MY 28  $L_S=42^\circ-84^\circ$  and MY 28  $L_S=85^\circ-127^\circ$  seasons, while the Viking mid-latitude phase function had the worst fit for the MY 28  $L_S=128-170^\circ$  season. This was to be expected as a majority of our data was confined to the latitude range of  $-20^\circ$  and  $+60^\circ$ , and the Viking observation period was unseasonably dusty (Tampaari et al., 2000).

Unfortunately, the viewing geometry and orbit of MRO during the PSP prevents us from observing the behaviour of MARCI-derived phase function curves at scattering angles below  $60^\circ$ . The shapes of the modeled curves at these smaller angles are much more varied and can help to better distinguish the prevalent geometries in the WICs observed. The fact that the MARCI phase function data was derived over a range of scattering angles where a majority of the phase functions converge, likely contributed to the higher p-values produced in this chi-squared

analysis, compared to the PFSS phase function. Furthermore, the aggregate ice crystal habit (which had the highest p-values of the seven modeled phase functions for all seasons in this work) does not produce a strong peak in its modeled phase function for randomly oriented ice crystals from Yang and Liou (1996) around the  $22^\circ$  and  $46^\circ$  scattering angles, which correspond to optical halos. This result agreed with our results from MSL and could be one possible reason why these scattering phenomena have yet to be observed on Mars.

Beyond the possibility of ice Ic dominating the observed Martian WICs, we were unable to determine a single property of Martian WICs from either of these analyses that would outright preclude the formation and/or observation of halos, parhelia and other scattering phenomena. If ice Ih dominates the clouds we observed, then we can only point to a few possible factors that would cumulatively make the intensity of the scattering phenomena difficult to detect, such as the increased scattering from dust aerosols in the Martian atmosphere, and partial sublimation of larger ice crystals like aggregates, which would dominate the scattered radiation signal.

# Chapter 7

## Conclusions

The annual recurrence of the ACB within  $-10^{\circ}$  and  $+30^{\circ}$  latitude (Wolff et al., 1999; Clancy et al. 1996) plays a role in the distribution of water in the Martian atmosphere, acting as a barrier to pole-ward transportation of water between the hemispheres. These clouds also contribute to the global radiation budget of Mars, and modelling the impact of these clouds from a radiative transfer perspective requires confidence in average cloud opacity, ice crystal habit, and particle size. While opacity is regularly monitored from the surface and orbit, constraining the shapes of the ice crystals is more difficult, but can be done by first constraining the scattering properties of the clouds via derivation of their average phase function. The goal of this work was to do just that from both the Martian surface and orbit by designing a new observation called the PFSS on MSL and using publicly available data from the Mars Color Imager aboard MRO. We observationally constrained the phase function of Martian WICs from the surface of Gale crater during the MY 34 ACB season and over a globally expanded range of Martian longitudes and latitudes in the MY 28 and 29 ACB seasons. This work also probed the  $180^{\circ}$  peak (also known as the opposition surge) to validate a Terrestrial empirical relationship for deriving IWC from water ice extinction or opacity from Dickinson et al. (2011), and to

compare the  $180^\circ$  HWHMs to those modeled by Chepfer et al. (2002), Yang and Liou, (1996) and Yang et al. (2010) for water ice crystals.

This study built upon Kloos et al. (2016), which produced a low-resolution lower bound of the phase function using MSL Navcam single-pointing cloud movies. A new Navcam sequence for MSL was designed and labeled the “Phase Function Sky Survey” in order to expand the range and resolution of scattering angles across the sky in each observation. The observation was then executed on an approximately weekly basis by MSL, alternating morning and evening observation times. In total, 35 observations were run over  $LS$   $61.9^\circ$ - $156.5^\circ$  and our results tripled the scattering angle range of  $41.7^\circ$  spanning from  $72.7^\circ$ - $114.4^\circ$  in Kloos et al. (2016), to a range of  $134.3^\circ$  spanning  $18.3^\circ$ - $152.6^\circ$ . The mean phase function derived from the PFSS data was normalized and compared with modeled phase functions of 7 ice crystal habits from Yang et al. (2010).

Through chi-squared probability tests, the five ice crystal geometries most likely to have been observed in the ACB Martian WICs were aggregates, hexagonal solid columns, hollow columns, plates, and bullet rosettes with p-values greater than or equal to 0.60, 0.57, 0.56, 0.56, and 0.55, respectively. Droxtals and spheres had p-values of 0.35, and 0.2, making them less probable components of Martian WICs, but still statistically possible ones.

Potential local maxima in the mean derived phase function curve at scattering angles  $\sim 22^\circ$ , and  $\sim 46^\circ$  could be evidence of scattering phenomena observed in terrestrial cirrus clouds such as  $22^\circ$  circular halos or parhelia,  $44^\circ$  parhelia,  $46^\circ$  halos, or supralateral arcs, if real. The modeled ice crystal geometries

with the highest p-values align with the production of these phenomena, however it is important to note that the models feature only randomly oriented crystals. While no features were detected by eye in our perturbation images, it's possible that the added optical depth and increased scattering from dust suspended in the Martian atmosphere could hinder human detection of these often diffuse and faint features. These results also agreed with observed  $180^\circ$  backscatter peaks in MARCI and MOC images and confirmation of observational detections of the backscatter peak by hexagonal plates and columns, and observed ice crystal geometries in terrestrial cirrus clouds.

Our results were compared with the relatively smooth and flat composite EPF and RT fit WIC phase functions from Clancy and Lee (1991) and Clancy and Wolff (2003) using a weighted chi-squared analysis and p-test. The Viking results from 1991 had p-values greater than or equal to 0.49 for mid-latitude clouds, and 0.48 for polar clouds, while the TES results from 2003 had p-values greater than or equal to 0.62 for type 1 aphelion clouds, and 0.60 for type 2 aphelion clouds.

For the orbital perspective, MARCI VIS filter data was downloaded from the PDS, calibrated, and run through a pipeline to select the pixels most likely to possess clouds, and calculate the phase function. The results were then compared to a dust event catalogue and analysis from Battalio and Wang (2019) to filter out any overlapping points and reduce contributions from dust in our data. The investigation period covered seasons  $L_S=42^\circ$ - $170^\circ$  in MYs 28 and 29 (MRO reached Mars at  $\sim L_S=128^\circ$  in MY28), and unnormalized phase function data points were plotted with respect scattering angle for each of the five filters. A geographic

analysis showed that the blue filter data was the least contaminated by Martian dust and surface features (compared to the longer wavelength filters), and thus was the best choice for the ice crystal habit analysis in Section 6.2. The green filter data was also utilized alongside the blue filter for the opposition surge analyses of Section 6.1 in order to compare to the green and blue MARCI filter  $180^\circ$  HWHMs of Cooper and Moores (2019).

In testing the empirical relationship from Dickinson et al. (2011) that IWC is equal to a factor of 10 multiplied by the water ice extinction, we utilized the mean phase functions from the  $180^\circ$  scattering angle bins for the blue filter and found that the column IWC was equal to opacity multiplied by a factor of 5 for the average 20 micron particles at the Phoenix landing site, and 0.7 for the average 2.75 micron particles of ACB clouds. Thus, we found that there is a large dependence of IWC on particle size, and so a general empirical relationship for all ice crystals on Mars is not applicable. For the HWHM of the opposition surge investigations, we had results within the range of values expected for WICs (approximately  $2^\circ$  -  $5^\circ$ ; Chepfer et al., 2002; Yang and Liou, 1996; Yang et al., 2010), compared to values for the Martian dust or the surface (on the order of  $10^\circ$  or greater; Clancy et al., 2003 and Soderblom et al., 2006).

A seasonal ice crystal habit analysis in the blue filter was completed to determine how the phase function changed with solar longitude (averaged over all latitudes and longitudes) by dividing the data into seasons ( $L_S=42^\circ$ - $84^\circ$ ,  $L_S=85^\circ$ - $127^\circ$ ,  $L_S=128^\circ$ - $170^\circ$  for each MY). The mean seasonal blue filter phase functions were normalized and compared to the seven modeled ice crystal phase functions from

Yang and Liou (1996) and Yang et al. (2010), along with the observationally derived phase function from the PFSS and the six RT-fit phase functions from Clancy and Lee, (1991) and Clancy et al., (2003). For all seasons, the ice crystal geometries most probably observed within the MARCI data were aggregates (with p-values ranging from 0.771 - 0.869) closely followed by bullet rosettes and solid columns, while the least likely were spheres (0.219 – 0.277). Droxtals had greater probabilities for this data set than the MSL data, with an average p-value of 0.699, compared to 0.35 previously. For the previously derived Martian WIC phase functions, the aphelion ice 1 from Clancy et al. (2003) had the greatest agreement (p-values ranging from 0.829 to 0.921) for all seasons except MY 29  $L_S=42^\circ-84^\circ$ , which best fit the PFSS phase function with a p-value of 0.866. The p-values for the phase functions from Clancy and Lee (1991) and Clancy et al. (2003) were higher for this data set than the data from the PFSS, with ranges from 0.806 to 0.921, compared to a range of 0.48 to 0.62 previously.

Similar to the MSL investigations from the surface, this perspective found relatively high probabilities of Martian WICs containing ice crystal habits that should produce scattering phenomena such as halos, parhelia, and arcs, but to this day, the opposition surge is the only confirmed scattering phenomenon that has been observed on Mars. It is possible that another type of water ice (ice Ic), which was put forward by Clancy et al. (2003) as the potential form of their seasonal ice aerosol type (which also had a good fit to our results), could be precluding the formation of these scattering phenomena, or if they do exist, their detection has been prevented by a combination of scattering from atmospheric dust, or a signal

dominated by aggregates with typically larger radii and partially sublimated irregular crystals possessing at the lower levels of WICs.

# Bibliography

Acton, Charles H., Jr., Ancillary data services of NASA's Navigation and Ancillary Information Facility, *Planet. Space Sci.*, Vol. 44, No. 1, pp 65-70, 1996.

ASTM G173-03 (2012), Standard Tables for Reference Solar Spectral Irradiances: Direct Normal and Hemispherical on 37° Tilted Surface, ASTM International, West Conshohocken, PA, 2012, [www.astm.org](http://www.astm.org)

Battalio, Michael, and Huiqun Wang. "The Aonia-Solis-Valles Dust Storm Track in the Southern Hemisphere of Mars." *Icarus* 321 (2019): 367-78.  
doi:10.1016/j.icarus.2018.10.026.

Bell, J. F., M. J. Wolff, M. C. Malin, W. M. Calvin, B. A. Cantor, M. A. Caplinger, R. T. Clancy, K. S. Edgett, L. J. Edwards, J. Fahle, F. Ghaemi, R. M. Haberle, A. Hale, P. B. James, S. W. Lee, T. McConnochie, E. Noe Dobrea, M. A. Ravine, D. Schaeffer, K. D. Supulver, and P. C. Thomas. "Mars Reconnaissance Orbiter Mars Color Imager (MARCI): Instrument Description, Calibration, and Performance." *Journal of Geophysical Research* 114, no. E8 (2009). doi:10.1029/2008je003315.

Benson, Jennifer L., David M. Kass, Armin Kleinböhl, Daniel J. McCleese, John T. Schofield, and Fredric W. Taylor. "Mars South Polar Hood as Observed by the Mars Climate Sounder." *Journal of Geophysical Research* 115, no. E12 (2010).  
doi:10.1029/2009je003554.

Chepfer, Helene, Patrick Minnis, David Young, Louis Nguyen, and Robert F. Arduini. "Estimation of Cirrus Cloud Effective Ice Crystal Shapes Using Visible

Reflectances from Dual-satellite Measurements." *Journal of Geophysical Research: Atmospheres* 107, no. D23 (2002). doi:10.1029/2000jd000240.

Clancy, R. Todd, Michael J. Wolff, Bruce A. Cantor, Michael C. Malin, and Timothy I. Michaels. "Valles Marineris Cloud Trails." *Journal of Geophysical Research* 114, no. E11 (2009). doi:10.1029/2008je003323.

Clancy, R. Todd, Michael J. Wolff, Philip R. Christensen. "Mars Aerosol Studies with the MGS TES Emission Phase Function Observations: Optical Depths, Particle Sizes, and Ice Cloud Types versus Latitude and Solar Longitude." *Journal of Geophysical Research* 108, no. E9 (2003). doi:10.1029/2003je002058.

Clancy, R. Todd, and Steven W. Lee. "A New Look at Dust and Clouds in the Mars Atmosphere: Analysis of Emission-phase-function Sequences from Global Viking IRTM Observations." *Icarus* 93, no. 1 (1991): 135-58. doi:10.1016/0019-1035(91)90169-t.

Cooper, Brittney, and John Moores. "A Surprising and Colorful Martian Scattering Artifact." *Research Notes of the AAS*, vol. 3, no. 2, 2019, p. 40., doi:10.3847/2515-5172/ab082a.

Cooper, Brittney A., John E. Moores, Douglas J. Ellison, Jacob L. Kloos, Christina L. Smith, Scott D. Guzewich, and Charissa L. Campbell. "Constraints on Mars Aphelion Cloud Belt Phase Function and Ice Crystal Geometries." *Planetary and Space Science* 168 (2019): 62-72. doi:10.1016/j.pss.2019.01.005.

Dickinson, C., L. Komguem, J.a. Whiteway, M. Illnicki, V. Popovici, W. Junkermann, P. Connolly, and J. Hacker. "Lidar Atmospheric Measurements on Mars

and Earth." *Planetary and Space Science* 59, no. 10 (2011): 942-51.

doi:10.1016/j.pss.2010.03.004.

Eliason, E. M., Lavoie, S. K., & Soderblom, L. A. (1996). The Imaging Node for the Planetary Data System. *Planetary and Space Science*, 44(1), 23-32.

doi:10.1016/0032-0633(95)00103-4

Ebert, Elizabeth E., and Judith A. Curry. "A Parameterization of Ice Cloud Optical Properties for Climate Models." *Journal of Geophysical Research* 97, no. D4 (1992): 3831. doi:10.1029/91jd02472.

Guzewich, Scott D., C. E. Newman, M. D. Smith, J. E. Moores, C. L. Smith, C. Moore, M. I. Richardson, D. Kass, A. Kleinböhl, M. Mischna, F. J. Martín-Torres, M.-P. Zorzano-Mier, and M. Battalio. "The Vertical Dust Profile Over Gale Crater, Mars." *Journal of Geophysical Research: Planets* 122, no. 12 (2017): 2779-792.

doi:10.1002/2017je005420.

Gooding, James L. (1986). Martian dust particles as condensation nuclei: A preliminary assessment of mineralogical factors. *Icarus*, 66(1), 56-74.

doi:10.1016/0019-1035(86)90006-0

Guzewich, Scott D., C. E. Newman, M. D. Smith, J. E. Moores, C. L. Smith, C. Moore, M. I. Richardson, D. Kass, A. Kleinböhl, M. Mischna, F. J. Martín-Torres, M.-P. Zorzano-Mier, and M. Battalio. "The Vertical Dust Profile Over Gale Crater, Mars." *Journal of Geophysical Research: Planets* 122, no. 12 (2017): 2779-792.

doi:10.1002/2017je005420.

Guzewich, Scott D., Michael D. Smith, and Michael J. Wolff. "The Vertical Distribution of Martian Aerosol Particle Size." *Journal of Geophysical Research: Planets* 119, no. 12 (2014): 2694-708. doi:10.1002/2014je004704.

Greenler, Robert. *Rainbows, Halos, and Glories*. Cambridge University Press., 1980.

Heymsfield, Andrew J., and Larry M. Miloshevich. "Relative Humidity and Temperature Influences on Cirrus Formation and Evolution: Observations from Wave Clouds and FIRE II." *Journal of the Atmospheric Sciences* 52, no. 23 (1995): 4302-326. doi:10.1175/1520-0469(1995)0522.0.co;2.

James, P. B., Pierce, M., & Martin, L. J. (1987). Martian north polar cap and circumpolar clouds: 1975–1980 telescopic observations. *Icarus*, 71(2), 306-312. doi:10.1016/0019-1035(87)90155-2

Johnson, Jeffrey R., William M. Grundy, and Mark T. Lemmon. "Dust Deposition at the Mars Pathfinder Landing Site: Observations and Modeling of Visible/near-infrared Spectra." *Icarus* 163, no. 2 (2003): 330-46. doi:10.1016/s0019-1035(03)00084-8.

Können, G.P. "A Halo on Mars." *Weather* 62, no. 6 (2007): 166-67. doi:10.1002/wea.100.

Kleinböhl, Armin, A. James Friedson, and John T. Schofield. "Two-dimensional Radiative Transfer for the Retrieval of Limb Emission Measurements in the Martian Atmosphere." *Journal of Quantitative Spectroscopy and Radiative Transfer* 187 (2017): 511-22. doi:10.1016/j.jqsrt.2016.07.009.

Kleinböhl, Armin, John T. Schofield, David M. Kass, Wedad A. Abdou, Charles R. Backus, Bhaswar Sen, James H. Shirley, W. Gregory Lawson, Mark I. Richardson, Fredric W. Taylor, Nicholas A. Teanby, and Daniel J. McCleese. "Mars Climate Sounder Limb Profile Retrieval of Atmospheric Temperature, Pressure, and Dust and Water Ice Opacity." *Journal of Geophysical Research: Planets* 114, no. E10 (2009). doi:10.1029/2009je003358.

Kleinböhl, Armin, John T. Schofield, Wedad A. Abdou, Patrick G.j. Irwin, and Remco J. De Kok. "A Single-scattering Approximation for Infrared Radiative Transfer in Limb Geometry in the Martian Atmosphere." *Journal of Quantitative Spectroscopy and Radiative Transfer* 112, no. 10 (2011): 1568-580.  
doi:10.1016/j.jqsrt.2011.03.006.

Kloos, J. L., J. E. Moores, J. A. Whiteway, and M. Aggarwal. "Interannual and Diurnal Variability in Water Ice Clouds Observed from MSL Over Two Martian Years." *Journal of Geophysical Research: Planets* 123, no. 1 (2018): 233-45.  
doi:10.1002/2017je005314.

Kloos, Jacob L., John E. Moores, Mark Lemmon, David Kass, Raymond Francis, Manuel De La Torre Juárez, María-Paz Zorzano, and F. Javier Martín-Torres. "The First Martian Year of Cloud Activity from Mars Science Laboratory (sol 0–800)." *Advances in Space Research* 57, no. 5 (2016): 1223-240.  
doi:10.1016/j.asr.2015.12.040.

Lemmon, Mark T., Joseph Michael Battalio, Manuel De La Torre Juarez, Javier Martín-Torres, Emily L Mason, Claire E Newman and Maria-Paz Zorzano. "Extinction measurements of dust aerosol from Mars Science Laboratory solar images."

*American Geophysical Union Fall Meeting*, 12-16 Dec 2016, San Francisco, CA. P21B-2082 .

Lemmon, Mark T., Michael J. Wolff, James F. Bell, Michael D. Smith, Bruce A. Cantor, and Peter H. Smith. "Dust Aerosol, Clouds, and the Atmospheric Optical Depth Record over 5 Mars Years of the Mars Exploration Rover Mission." *Icarus* 251 (2014): 96-111. doi:10.1016/j.icarus.2014.03.029.

Lemmon, M. T. "Atmospheric Imaging Results from the Mars Exploration Rovers: Spirit and Opportunity." *Science* 306, no. 5702 (2004): 1753-756. doi:10.1126/science.1104474.

Liou, Kuo-Nan. *An Introduction to Atmospheric Radiation, Second Edition*. Academic Press., 2002.

Madeleine, J.-B., F. Forget, A. Spiga, M. J. Wolff, F. Montmessin, M. Vincendon, D. Jouglet, B. Gondet, J.-P. Bibring, Y. Langevin, and B. Schmitt. "Aphelion Water-ice Cloud Mapping and Property Retrieval Using the OMEGA Imaging Spectrometer Onboard Mars Express." *Journal of Geophysical Research: Planets* 117, no. E11 (2012). doi:10.1029/2011je003940.

Maki, J., D. Thiessen, A. Pourangi, P. Kobzeff, T. Litwin, L. Scherr, S. Elliott, A. Dingizian, and M. Maimone. "The Mars Science Laboratory Engineering Cameras." *Mars Science Laboratory*, (2012), 77-93. doi:10.1007/978-1-4614-6339-9\_5.

Malin, M. C., Bell, J. F., Calvin, W., Clancy, R. T., Haberle, R. M., James, P. B., . . . Caplinger, M. A. (2001). Mars Color Imager (MARCI) on the Mars Climate Orbiter. *Journal of Geophysical Research: Planets*, 106(E8), 17651-17672. doi:10.1029/1999je001145

Maltagliati, L., F. Montmessin, A. Fedorova, O. Korablev, F. Forget, and J.-L. Bertaux. "Evidence of Water Vapor in Excess of Saturation in the Atmosphere of Mars." *Science* 333, no. 6051 (2011): 1868-871. doi:10.1126/science.1207957.

Mars Science Laboratory (MSL) Software Interface Specification. "Camera & LIBS Experiment Data Record (EDR) and Reduced Data Record (RDR) Data Products." (2015).

Miller, N., Juárez, M. D., & Tamppari, L. (2018). The Effect of Bagnold Dunes Slopes on the Short Timescale Air Temperature Fluctuations at Gale Crater on Mars. *Geophysical Research Letters*, 45(21). doi:10.1029/2018gl080542

Montabone, L., F. Forget, E. Millour, R.j. Wilson, S.r. Lewis, B. Cantor, D. Kass, A. Kleinböhl, M.t. Lemmon, M.d. Smith, and M.j. Wolff. "Eight-year Climatology of Dust Optical Depth on Mars." *Icarus* 251 (2015): 65-95. doi:10.1016/j.icarus.2014.12.034.

Montmessin, F., F. Forget, P. Rannou, M. Cabane, and R. M. Haberle. "Origin and Role of Water Ice Clouds in the Martian Water Cycle as Inferred from a General Circulation Model." *Journal of Geophysical Research* 109, no. E10 (2004). doi:10.1029/2004je002284.

Moores, John E. and 24 Co-Authors. "Atmospheric Movies Acquired at the Mars Science Laboratory Landing Site: Cloud Morphology, Frequency and Significance to the Gale Crater Water Cycle and Phoenix Mission Results." *Advances in Space Research* 55, no. 9 (2015): 2217-238. doi:10.1016/j.asr.2015.02.007.

Moores, John E., Léonce Komguem, James A. Whiteway, Mark T. Lemmon, Cameron Dickinson, and Frank Daerden. "Observations of Near-surface Fog at the

Phoenix Mars Landing Site." *Geophysical Research Letters* 38, no. 4 (2011).

doi:10.1029/2010gl046315.

Moore, John E., Mark T. Lemmon, Peter H. Smith, Leonce Komguem, and James A. Whiteway. "Atmospheric Dynamics at the Phoenix Landing Site as Seen by the Surface Stereo Imager." *Journal of Geophysical Research* 115 (2010).

doi:10.1029/2009je003409.

Moore, John., Smith, P., Tanner, R., Schuerger, A., & Venkateswaran, K. (2007). The shielding effect of small-scale Martian surface geometry on ultraviolet flux. *Icarus*, 192(2), 417-433. doi:10.1016/j.icarus.2007.07.003

Petrosyan, A., B. Galperin, S. E. Larsen, S. R. Lewis, A. Määttänen, P. L. Read, N. Renno, L. P. H. T. Rogberg, H. Savijärvi, T. Siili, A. Spiga, A. Toigo, and L. Vázquez. "The Martian Atmospheric Boundary Layer." *Reviews of Geophysics* 49, no. 3 (2011). doi:10.1029/2010rg000351.

Poetsch-Heffter, C., Q. Liu, E. Ruperecht, and C. Simmer. "Effect of Cloud Types on the Earth Radiation Budget Calculated with the ISCCP Cl Dataset: Methodology and Initial Results." *Journal of Climate* 8, no. 4 (1995): 829-43. doi:10.1175/1520-0442(1995)0082.0.co;2.

Pollack, James B., David S. Colburn, F. Michael Flasar, Ralph Kahn, C. E. Carlston, and D. Pidek. "Properties and Effects of Dust Particles Suspended in the Martian Atmosphere." *Journal of Geophysical Research* 84, no. B6 (1979): 2929. doi:10.1029/jb084ib06p02929.

Rohatgi, Ankit Rohatgi. WebPlotDigitizer. Version 4.1. January 2018. <https://automeris.io/WebPlotDigitizer>.

Ruff, Steven W., & Christensen, P. R. (2002). Bright and dark regions on Mars: Particle size and mineralogical characteristics based on Thermal Emission Spectrometer data. *Journal of Geophysical Research: Planets*, 107(E12). doi:10.1029/2001je001580

Schlimme, I., A. Macke, and J. Reichardt. "The Impact of Ice Crystal Shapes, Size Distributions, and Spatial Structures of Cirrus Clouds on Solar Radiative Fluxes." *Journal of the Atmospheric Sciences* 62, no. 7 (2005): 2274-283. doi:10.1175/jas3459.1.

Simon, J., P. Bretagnon, J. Chapront, M. Chapront-Touze, G. Francou, and J. Laskar. "Numerical Expressions for Precession Formulae and Mean Elements for the Moon and the Planets." *Astronomy and Astrophysics* 282, no. 2 (February 1994): 663-83.

Smith, Michael D. "THEMIS Observations of Mars Aerosol Optical Depth from 2002–2008." *Icarus* 202, no. 2 (2009): 444-52. doi:10.1016/j.icarus.2009.03.027.

Smith, Peter H., and Mark Lemmon. "Opacity of the Martian Atmosphere Measured by the Imager for Mars Pathfinder." *Journal of Geophysical Research: Planets* 104, no. E4 (1999): 8975-985. doi:10.1029/1998je900017.

Soderblom, Jason., Bell III, J., Hubbard, M., & Wolff, M. (2006). Martian phase function: Modeling the visible to near-infrared surface photometric function using HST-WFPC2 data. *Icarus*, 184(2), 401-423. doi:10.1016/j.icarus.2006.05.006

Tamppari, Leslie K. "Viking-era Diurnal Water-ice Clouds." *Journal of Geophysical Research* 108, no. E7 (2003). doi:10.1029/2002je001911.

Vasavada, A.R., S. Piqueux, K.W. Lewis, M.T. Lemmon, and M.D. Smith.  
"Thermophysical properties along Curiosity's traverse in Gale crater, Mars, derived from the REMS Ground Temperature Sensor." *Icarus* 284, (2017) 372-386. doi: 10.1016/j.icarus.2016.11.035.

Vincendon, M., Audouard, J., Altieri, F., & Ody, A. (2015). Mars Express measurements of surface albedo changes over 2004–2010. *Icarus*, 251, 145-163. doi:10.1016/j.icarus.2014.10.029

Wang, Huiqun. "Martian Clouds Observed by Mars Global Surveyor Mars Orbiter Camera." *Journal of Geophysical Research* 107, no. E10 (2002). doi:10.1029/2001je001815.

Wang, Chenxi, Ping Yang, Andrew Dessler, Bryan A. Baum, and Yongxiang Hu. "Estimation of the Cirrus Cloud Scattering Phase Function from Satellite Observations." *Journal of Quantitative Spectroscopy and Radiative Transfer* 138 (2014): 36-49. doi:10.1016/j.jqsrt.2014.02.001.

Wang, Huiqun, Michael Battalio, and Zachary Huber. MARS MRO MARCI Mars Daily Global Maps Archive | USGS Astrogeology Science Center. Accessed May 15, 2019. <https://astrogeology.usgs.gov/search/map/Mars/MarsReconnaissanceOrbiter/MARCI/MARS-MRO-MARCI-Mars-Daily-Global-Maps>.

Wang, Huiqun, & Richardson, M. I. (2015). The origin, evolution, and trajectory of large dust storms on Mars during Mars years 24–30 (1999–2011). *Icarus*, 251, 112-127. doi:10.1016/j.icarus.2013.10.033

Whiteway, J. A. and 23 Co-Authors. "Mars Water-Ice Clouds and Precipitation." *Science* (2009) 68–70. doi: 10.1126/science.1172344.

Whiteway, James, Clive Cook, Martin Gallagher, Tom Choullarton, John Harries, Paul Connolly, Reinhold Busen, Keith Bower, Michael Flynn, Peter May, Robin Aspey, and Jorg Hacker. "Anatomy of Cirrus Clouds: Results from the Emerald Airborne Campaigns." *Geophysical Research Letters*, vol. 31, no. 24, 2004, doi:10.1029/2004gl021201.

Wilson, R. John, Gregory A. Neumann, and Michael D. Smith. "Diurnal Variation and Radiative Influence of Martian Water Ice Clouds." *Geophysical Research Letters* 34, no. 2 (2007). doi:10.1029/2006gl027976.

Wolff, M. J., M. D. Smith, R. T. Clancy, R. Arvidson, M. Kahre, F. Seelos, S. Murchie, and H. Savijärvi. "Wavelength Dependence of Dust Aerosol Single Scattering Albedo as Observed by the Compact Reconnaissance Imaging Spectrometer." *Journal of Geophysical Research* 114 (2009). doi:10.1029/2009je003350.

Wolff, Michael J., James F. Bell, Philip B. James, R. Todd Clancy, and Steven W. Lee. "Hubble Space Telescope Observations of the Martian Aphelion Cloud Belt Prior to the Pathfinder Mission: Seasonal and Interannual Variations." *Journal of Geophysical Research: Planets* 104, no. E4 (1999): 9027-041. doi:10.1029/98je01967.

Yang, Ping, Gang Hong, Andrew E. Dessler, Steve S. C. Ou, Kuo-Nan Liou, Patrick Minnis, and Harshvardhan. "Contrails and Induced Cirrus." *Bulletin of the*

*American Meteorological Society* 91, no. 4 (2010): 473-78.

doi:10.1175/2009bams2837.1.

Yang, Ping, Bryan A. Baum, Andrew J. Heymsfield, Yong X. Hu, Hung-Lung Huang, Si-Chee Tsay, and Steve Ackerman. "Single-scattering Properties of Droxtals." *Journal of Quantitative Spectroscopy and Radiative Transfer* 79-80 (2003): 1159-169. doi:10.1016/s0022-4073(02)00347-3.

Yang, Ping, and K. N. Liou. "Geometric-optics–integral-equation Method for Light Scattering by Nonspherical Ice Crystals." *Applied Optics* 35, no. 33 (1996): 6568. doi:10.1364/ao.35.006568.

Zhou, Chen, and Ping Yang. "Backscattering Peak of Ice Cloud Particles." *Optics Express* 23, no. 9 (2015): 11995. doi:10.1364/oe.23.011995.

Zurek, Richard W., and Suzanne E. Smrekar. "An Overview of the Mars Reconnaissance Orbiter (MRO) Science Mission." *Journal of Geophysical Research* 112, no. E5 (2007). doi:10.1029/2006je002701.